AUTONOMOUS MEASUREMENT OF PHYSICALLY AND BIOLOGICALLY DRIVEN CHANGES IN DISSOLVED OXYGEN IN THE NORTHERN GULF OF MEXICO

by

Christopher Gordon

Submitted in partial fulfillment of the requirements
for the degree of Master of Science

at

Dalhousie University
Halifax, Nova Scotia
December 2019

TABLE OF CONTENTS

LIST OF TABLES

LIST OF FIGURES

ABSTRACT

Oceanic primary production is an important quantity that has both oceanographic and societal impacts. It forms the basis of the marine food web, and provides a pathway for carbon to be sequestered in the oceans interior. Despite its importance, the spatial and temporal variation of primary production in the ocean is poorly observed. This is in part because techniques for measuring production are often difficult and laborious. However, the emergence of miniaturized biogeochemical sensors and their integration into piloted and autonomous platforms such as gliders and profiling floats has opened new avenues for measuring primary production. In this thesis, I attempt to estimate primary production from measured diurnal changes in dissolved oxygen concentration in the upper ocean that were obtained by autonomous floats deployed in the northern Gulf of Mexico. I first examine whether profiling floats are a capable platform to measure diurnal changes in oxygen, and develop a novel method for correcting oxygen sensor response time in-situ. Then I characterize the various drivers, both physical and biological, that influence oxygen in this region, and evaluate if the diurnal biological signal can be observed. Analysis of the measurements is combined with a simple, one-dimensional numerical model to examine the relationship between sampling rate, sensor accuracy, and resulting estimates of primary production.

List of Abbreviations and Symbols Used

A Vertical velocity Gaussian height parameter / [$m^2\ d^{-1}$]

G Mean float gain value / [unitless]

X_{O_2} Molar fraction of oxygen in air / [unitless]

ϵ Simulated random sensor error / [mmol $O_2\ m^{-3}$]

$\mathrm{pH_2O}$ Vapor pressure of water / [kPa]

$\mathrm{pO_2}$ Oxygen partial pressure calculated from reanalysis / [kPa]

$\mathrm{pO_{2\ optode}}$ Oxygen partial pressure measured by oxygen optode / [kPa]

μ_τ Mean value of the simulated distribution of sensor response times / [s]

ω Vertical velocity oscillation frequency / [d^{-1}]

σ Vertical velocity Gaussian width parameter / [m]

σ_G Standard deviation of oxygen gain values / [unitless]

σ_ϵ Standard deviation of the simulated distribution of random sensor error / [mmol $O_2\ m^{-3}$]

σ_τ Standard deviation of the simulated distribution of sensor response times / [s]

σ_τ Standard deviation of oxygen response time values / [s]

σ_{dev} Standard deviation of the deviation of simulated profiles from the truth given response time or random sensor error / [mmol $O_2\ m^{-3}$]

τ Oxygen optode response time / [s]

g_i Single in-air gain value / [unitless]

k_D Diffusion coefficient / [d^{-1}]

m Manufacturer-provided slope for converting fluorometer measurements (counts) to chlorophyll concentration (mg m^{-3}) / [mg m^{-3}]

p p-value statistic / [unitless]

r Correlation coefficient / [unitless]

t_0 Vertical velocity oscillation offset time / [d]

w Vertical velocity / [m d^{-1}]

z_0 Vertical velocity Gaussian central depth parameter / [m]

Biogeochemical (BGC)

Carbon-based Production Model (CbPM)

Coloured Dissolved Organic Matter (CDOM)

Conductivity Temperature Depth sensor (CTD)

Deep Chlorophyll Maximum (DCM)

Dissolved Inorganic Carbon (DIC)

ElectroMagnetic Autonomous Profiling EXplorer (EM-APEX)

Gross Oxygen Production (GOP)

Gross Primary Production (GPP)

Light-emitting Diode (LED)

Model Experiments (ME)

Mixed Layer Depth (MLD)

National Centers for Environmental Protection (NCEP)

Net Community Production (NCP)

Net Primary Production (NPP)

Non-photochemical Quenching (NPQ)

Photosynthetically Active Radiation (PAR)

Particulate Organic Carbon (POC)

Root Mean Square Difference (RMSD)

Regional Ocean Modeling System (ROMS)

Respiration (R)

Southern Ocean Carbon and Climate Observations and Modelling (SOCCOM)

Vertically Generalized Production Model (VGPM)

Volume Scattering Function (VSF)

World Ocean Atlas (WOA)

ACKNOWLEDGEMENTS

I would first like the thank my supervisor, Dr. Katja Fennel, from whom I have learned so much. Thanks to my committee members, Dr. Marlon Lewis and Dr. Keith Thompson for their invaluable input and feedback throughout my degree. I would like to thank past and present members of the Marine Environmental Modelling Group, and the Dalhousie department of Oceanography graduate student community. Finally I would like to thank my family and friends for their support thoughout, especially Alex Brown, Andrew Johnston, Garrett Jung, Jennie Korus, Katie Gordon, Krysten Rutherford, Kyle Chapman, Makenzie Gallagher, Sara Sparavalo, and my parents John and Michele Gordon.

CHAPTER 1

INTRODUCTION

Oceanic primary production is a fundamentally important process with implications for a wide array of research topics and relevance to society. Primary production, the growth of organic material through photosynthesis, forms the basis of the oceanic food web and supports higher trophic levels. It is also a major component of the global carbon cycle, providing a pathway for carbon to be sequestered in the deep ocean, and thus is vital to our understanding of climate change.

Although primary production is intrinsic to understanding biogeochemical dynamics in the ocean, its temporal and spatial variability is not well observed. This is in part because production is not easily measured. Historically, production has been estimated by performing bottle incubations using isotopically marked carbon-14 (^{14}C) (*Steeman-Nielsen*, 1952). In this method, the initial concentration of Dissolved Inorganic Carbon (DIC) in a water sample is measured (or the value is assumed), then a known amount of heavier ^{14}C-DIC is added. After an incubation period (typically 24 h, but can vary), the amount of labelled carbon that has been assimilated into organic matter is measured. With these known quantities, a calculation of the total carbon uptake can be performed, thus deriving production. These incubations require substantial effort and expensive ship time, while only providing point estimates of production.

Satellites offer a path to estimating production on an expansive spatial scale, but under the burden of large assumptions, including local light intensity, the parameters of the photosynthesis-irradiance relationship, and the vertical structure of biomass. Satellites measure surface ocean reflectances across several spectral bands, i.e. ocean color, from which surface-ocean concentrations of chlorophyll and Particulate Organic Carbon (POC)

can be estimated. Algorithms for converting surface chlorophyll concentrations or POC (in $mg\,m^{-3}$) to vertically integrated production estimates (in $mg\ C\,m^{-2}\,d^{-1}$), e.g. the Vertically Generalized Production Model (VGPM, *Behrenfeld and Falkowski*, 1997) or Carbon-based Production Model (CbPm, *Westberry et al.*, 2008), rely heavily on assumptions about the subsurface and use global regressions of observed productivity with sea surface temperature.

Both of the above methods quantify Net Primary Production (NPP). NPP is defined as the total rate of carbon fixed by photosynthesizing organisms, minus autotropic respiration. The total carbon fixed is referred to as Gross Primary Production (GPP). Other methods for estimation of production consider the whole planktonic community and consider losses due to both autotrophic and heterotrophic respiration. Community Respiration (R) is the total rate of fixed carbon respired by autotrophs and heterotrophs to meet their energy needs. The balance between Gross Primary Production and Community Respiration in the upper ocean is referred to as the Net Community Production (NCP) and represents the net rate of biomass production ($NCP = GPP - R$) by the biological community which is either expressed as increased biomass or in exported carbon.

NCP in the mixed layer can be estimated by measuring the ratio of dissolved oxygen to dissolved argon ($[O_2]/[Ar]$) (*Kaiser et al.*, 2005; *Cassar et al.*, 2009; *Hamme et al.*, 2012; *Tortell et al.*, 2014). The two gases have similar physical properties with regard to their solubility, but Ar is biologically inactive while oxygen is produced and consumed by production and respiration. In other words, the two gases are affected very similarly by any physical processes, but only O_2 is subject to biological processes. The ratio of $[O_2]/[Ar]$ thus can be used to partition changes in oxygen into physical and biological components, where the biological component represents NCP. The change ratio of oxygen to argon concentrations relative to their saturation ratio ($\Delta[O_2]/[Ar]$) is calculated by measuring the in-situ concentrations of O_2 and Ar using mass-spectroscopy, dividing by their saturation concentrations and subtracting 1 ($\Delta[O_2]/[Ar] = ([O_2]/\,[Ar])/([O_2]_{sat}\,/[Ar]_{sat}) - 1$). This quantity reflects biological processes and can be stoichiometrically converted to NCP representative for the timescale of mixed layer gas exchange, usually about 10 to 30 days. A positive $\Delta[O_2]/[Ar]$ is indicative of net production (positive NCP), and a negative of net respiration (negative NCP). This technique offers a better time-space resolution than ^{14}C incubations as mass-spectrometry can be applied in high-precision and continuously to

a seawater flow-through on a steaming ship. This makes the technique a good candidate for deployment on ships of opportunity, but the capability has not yet been extended to autonomous platforms.

The emergence of miniaturized biogeochemical sensors and their integration into piloted and autonomous platforms such as gliders and profiling floats have opened new avenues for measuring production. Numerous studies have used particulate beam attenuation (*Cullen et al.*, 1992; *Claustre et al.*, 1999; *Kinkade et al.*, 1999; *Gernez et al.*, 2010; *Dall'Olmo et al.*, 2011; *Omand et al.*, 2017; *White et al.*, 2017) or dissolved oxygen (*Caffrey*, 2003; *Riser and Johnson*, 2008; *Nicholson et al.*, 2015; *Briggs et al.*, 2018) to estimate production from sensors mounted on such platforms.

Riser and Johnson (2008) used profiling floats to measure oxygen profiles every 10 days in the subtropical Pacific Ocean. Oxygen below the mixed layer showed a steady increase throughout the stratified period indicating positive NCP. The slope of the buildup of oxygen allowed for an estimation of seasonally averaged NCP below the mixed layer.

Furthermore, GPP and R have been estimated from diurnal cycles of oxygen within the mixed layer observed by gliders (*Nicholson et al.*, 2015) and mixed layer floats (*Briggs et al.*, 2018). Diurnal analysis has also been performed using beam-c measurements from underway ship flow-through (*White et al.*, 2017). In *Nicholson et al.* (2015), approximately 14 glider profiles per day over a study period of 110 days were used to observe the diurnal cycle of dissolved oxygen within the mixed layer. These measurements were combined into an average diel cycle to determine GPP and NCP. The technique applied in *White et al.* (2017) and *Briggs et al.* (2018) also makes use of the diel cycle of biological production, but instead of averaging over many days to obtain an average diurnal cycle, uses the continuous measurements of a mixed layer float to observe daily diel cycles. In *Briggs et al.* (2018), by measuring the decline of dissolved oxygen through the night, the respiration rate R is determined. Then, by observing the subsequent increase of dissolved oxygen during daylight hours and subtracting R, Gross Oxygen Production (GOP) can be calculated. GOP is analogous to GPP, but in units of oxygen rather than carbon and can be converted to GPP.

While these initial results for deriving production from autonomous/piloted oxygen measurement platforms are encouraging, they either required large averaging periods or neglected at least some portion of the water column where production is likely to

occur. In this thesis, I seek to test whether diurnal cycles of vertically integrated dissolved oxygen can be observed with profiling floats to estimate productivity. I am using oxygen measurements from ten floats that were deployed in the Gulf of Mexico in 2017 and were directed to profile continuously for several days at a time. This work most directly extends previous research with autonomous floats by *Briggs et al.* (2018) by using profiling rather than mixed-layer floats and explicitly considering the entire euphotic zone. If feasible, this could provide estimates of production rates at much better spatial and temporal coverage than presently available.

With this objective in mind, my overarching research question is:

> Can GPP, R, and NCP be estimated from the diurnal oxygen cycle measured by continuously profiling autonomous floats?

To answer this overarching question, two sets of more specific questions, one technical and one oceanographic, are addressed first:

1. Are autonomous profiling floats capable of sampling at the rate and accuracy required to resolve diurnal scale changes in oxygen? What is the relationship between sampling rate, accuracy, and magnitude of NCP and R?

2. What are the primary physical or biological drivers of change in dissolved oxygen in the upper water column near the shelf break in the northern Gulf of Mexico? Are there physical processes that can confound the diurnal biological oxygen signal? If yes, can physical and biological processes be separated?

The first set of questions addresses technical aspects of the measurement. As profiling floats have not yet been used to measure diel variations of oxygen, it is necessary to determine if they are able to properly resolve the signal. While oxygen optodes have been shown to be reliable and stable when deployed on autonomous floats (*Tengberg et al.*, 2006; *Gruber et al.*, 2010), with only a weak drift of less than 1% per year (*Bushinsky et al.*, 2016; *Bittig and Körtzinger*, 2016), they are known to require pressure (*Bittig et al.*, 2015), in-air gain (*Johnson et al.*, 2015; *Nicholson and Feen*, 2017) and response time (*Bittig et al.*, 2014, 2018) corrections. The ability to reliably perform these corrections in order to extract highly accurate measurements from the optode will be paramount to measuring the diel oxygen signal.

The second set of research questions addresses the environmental side of measuring production autonomously *in-situ*. The shelf break region in the northern Gulf of Mexico is dynamic, with a large freshwater input from the Mississippi watershed leading to eutrophic conditions on the shelf, while the shelf break and open Gulf are oligotrophic with low rates of primary production. Given this, can the weak biological signal be separated from potential physical processes affecting water column oxygen? The first demonstration of diel oxygen cycle measurement by *Briggs et al.* (2018) was performed in the North Atlantic Ocean during the spring bloom where rates of production were up to 16 mmol O_2 m^{-3} d^{-1}, much higher than rates typically found in oligotrophic systems (e.g. an average productivity of 1.8 mmol O_2 m^{-3} d^{-1} measured by *Nicholson et al.* (2015) near the Hawaii Ocean Timeseries). To provide further context, annual average NPP in the open Gulf of Mexico is about 1/3 of that in the North Atlantic (Gulf of Mexico average of 28 mmol C m^{-2} d^{-1}, North Atlantic average of 78 mmol C m^{-2} d^{-1} from 2012-2015, per VGPM *Behrenfeld and Falkowski*, 1997). Smaller biological signals are likely more difficult to observe.

Analysis of measurements from ten autonomous floats deployed near the shelf break in the northern Gulf of Mexico, and of complementary one-dimensional (1D) model simulations will serve to answer the research questions. Quality control and correction of oxygen optode measurements is described and discussed in depth, and their accuracy is evaluated before attempting to isolate the biological diurnal cycle of dissolved oxygen. The possible drivers of oxygen variability in the upper ocean are explored, especially how physical processes can influence dissolved oxygen. The ways in which these processes manifest themselves in the oxygen measurements are discussed, and suggestions for recognizing and removing confounding signals to isolate the biological signal are given.

Analyses of the observations and numerical model results will be presented in parallel in this thesis to present a complete view of each research question. The viability of oxygen optodes for measuring vertically integrated diurnal changes is assessed by employing a simple model for optode response time to simulate how measurement and post-measurement correction may induce errors in the observations. A 1D biological model is used to simulate the diel oxygen cycle in order to examine how sampling frequency and sensor error may influence its manifestation in the measurements. The model will also be compared with the float observations to explicitly examine the interaction of physical processes and biological

production.

Overall, the research presented in this thesis will contribute to improved quality control of oxygen measurements by optodes, may stimulate the use of autonomous floats to observe diurnal cycles of dissolved oxygen for calculation of NCP and R, and enhance our understanding of the processes driving changes in oxygen in the shelf break region in the northern Gulf of Mexico. The methods and findings of this work are applicable to other regions.

CHAPTER 2

STUDY AREA

The Gulf of Mexico is a semi-enclosed basin south of the contiguous United States of America. To the east, the Gulf is connected to the Atlantic Ocean via the Florida Straits and through the Yucatan Channel. Originating from the Atlantic, the Loop Current carries warm, saline water into the Gulf, and sheds eddies that propagate westward across the Gulf carrying their distinct oceanographic properties with them. The open Gulf is an oligotrophic environment where primary production is nutrient-limited, while the shelf in the northern Gulf, where the Mississippi and Atchafalaya rivers drain large amounts of nutrients and freshwater, is a eutrophic environment, leading to widespread hypoxic conditions in the summer (*Bianchi et al.*, 2010; *Fennel et al.*, 2013b; *Yu et al.*, 2015) on the shelf.

The Gulf experiences episodic perturbations by hurricanes and tropical storms, particularly during September and October. These events have the potential to influence primary productivity as deep mixing disrupts the density stratification of the water column and may temporarily alleviate surface nutrient limitation.

The Gulf of Mexico is also a site of significant oil and gas exploration and extraction activities that can harm the surrounding ecosystem. A striking example of this was seen during the 2010 Deepwater Horizon oil spill. In addition to such rapid, catastrophic anthropogenic influences, the Gulf is under increasing pressure from ocean warming, acidification, and deoxygenation (*Bopp et al.*, 2013; *Boyd et al.*, 2015). On the whole, the Gulf of Mexico is a highly dynamic region under the influence of both natural and anthropogenic pressures.

Production rates in the open Gulf estimated by surface satellite measurements show a

seasonality with higher production of 450-800 mg C m^{-2} d^{-1} (38-66 mmol C m^{-2} d^{-1}) in the winter, and lower production of 200-400 mg C m^{-2} d^{-1} (17-34 mmol C m^{-2} d^{-1}) in the summer (*Muller-Karger et al.*, 2015). Production varies geographically across the Gulf; rates tend to be higher in the northwest and lower in the southeast. It should be noted that the seasonal trends in productivity replicate those of surface chlorophyll in the Gulf as chlorophyll is the primary input for the production calculation, thus these estimates do not account for possible seasonal changes in the subsurface.

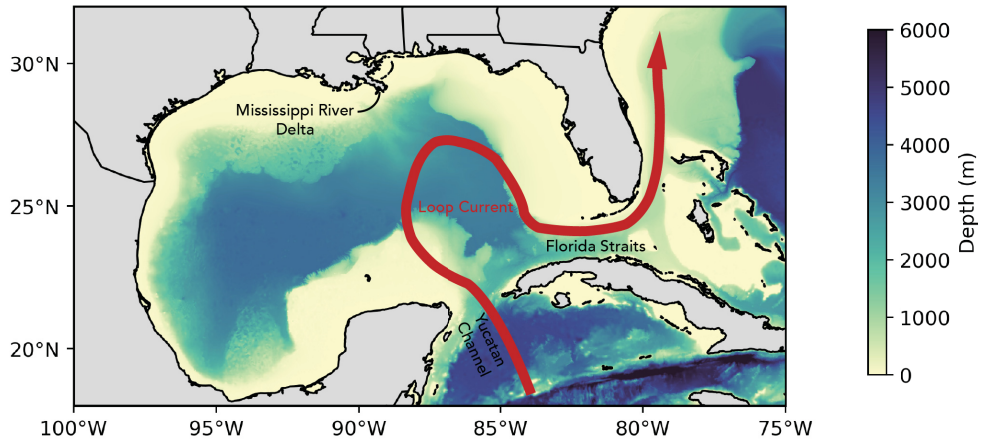

Figure 2.1: Bathymetric map of the Gulf of Mexico, showing the loop current enter through the Yucatan Channel and exit via the Florida Straits after intruding into the central Gulf. In the north the location of the Misssissippi River delta is shown, which supplies nutrients to the eutrophic northern shelf region.

Oxygen concentrations in the open Gulf never approach hypoxic levels; those are confined to near-bottom waters on the northern shelf. Typical oxygen profiles exhibit nearly constant oxygen concentrations throughout the mixed layer in near-equilibrium concentrations of about 200-220 mmol m^{-3}. Below the mixed layer, oxygen declines with depth to about 100 m and remains almost constant below that at about 140-160 mmol m^{-3}, but can increase slightly again at greater depths.

CHAPTER 3

METHODS

3.1 Float Functionality and Deployment

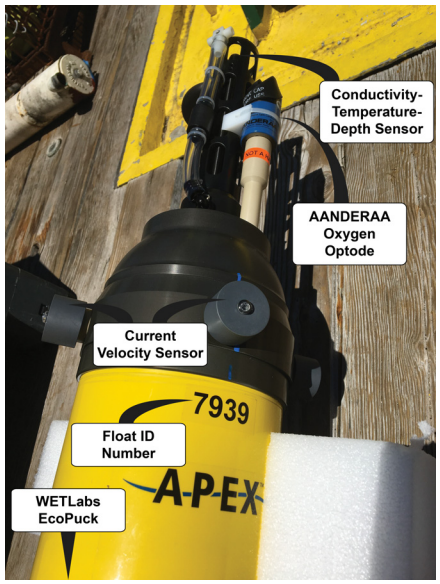

Figure 3.1: Photo of float f7939, one of the 10 autonomous EM-APEX floats with the various sensors labelled.

In May 2017, 10 autonomous EM-APEX floats (ElectroMagnetic-Autonomous Profiling EXplorer; Figure 3.1) were deployed in the northern Gulf of Mexico near the Mississippi delta (figure 3.2). The floats were equipped with a unique suite of sensors, including a Seabird Scientific Conductivity Temperature Depth sensor (CTD), 2 electromagnetic current velocity sensors (developed by Applied Physics Laboratory of the University of Washington), a WETLabs EcoPuck bio-optical triplet which measures chlorophyll fluorescence, optical backscattering and Coloured Dissolved Organic Matter (CDOM), and an Aanderaa 4330 oxygen optode. This study mostly uses data from the oxygen optode and CTD, and some data from the optical triplet. Current velocity measurements are not used here.

The floats operated in two different sampling modes: (1) the traditional "park-and-profile" mode where floats surfaced once every 5 or 10 days and drifted at 1000 m depth in between profiles, and (2) the "continuous" mode where floats were continuously profiling the top 1000 m, pausing only to transmit data at the surface following an upcast (this

resulted in one profile about every 3 hours). The sampling mode of the float was changed via two-way iridium satellite communication.

The floats were deployed in a grid (Figure 3.2 inset), and a set of discrete shipboard measurements was taken in conjunction with each deployment. The floats were initially set to continuous mode for about one week. After that, the floats were switched to park-and-profile mode until hurricanes Irma and Nate passed through the Gulf during which the floats were operated in continuous mode again. The complete dataset contains 3 periods of high frequency sampling for each float, i.e. after deployment and during the passage of each hurricane (see figure 3.3). The floats were usually not co-located with the hurricane path, but continuous mode profiling captured shorter time scale processes during elevated winds.

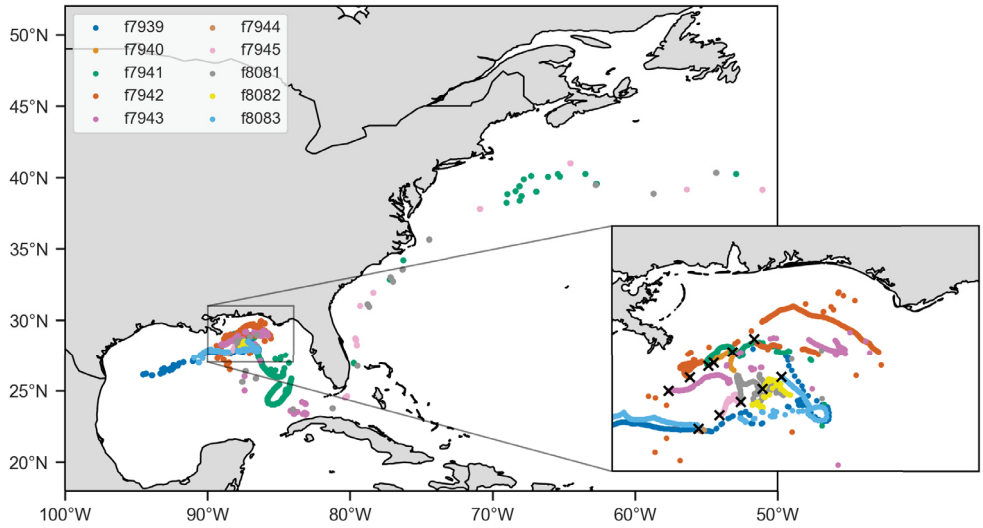

Figure 3.2: Map of deployment stations and float trajectories. The inset shows the 10 stations (black crosses) where shipboard measurements were made and floats deployed.

Three floats failed less than one month into the deployment. Although it is difficult to diagnose these failures without recovering the floats, the location data suggests that during the continuous mode sampling these floats had drifted near or onto shelf areas with low-density surface waters for which they were not properly ballasted. Without the required buoyancy to surface in these areas, the floats would have been trapped below the surface. One float showed evidence of a low-salinity plume during which it was not surfacing or transmitting data, but resumed functioning normally again later. Two more floats transmitted data until the end of 2017, and the remaining five floats operated until

summer of 2018, with the last transmission occurring on June 2, 2018. Three of the floats were entrained into the Loop Current and left the Gulf, eventually ending up in the North Atlantic (Figure 3.2).

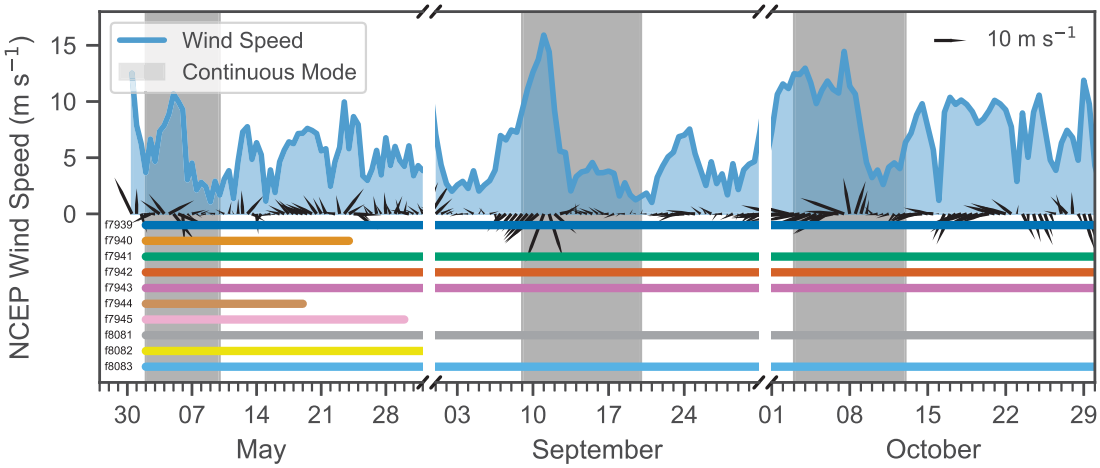

Figure 3.3: Timeseries of wind velocity (blue) and direction vectors (black arrows). Shaded areas show the times that the autonomous floats operated in continuous mode. Coloured lines below the timeseries show the duration of operation of each float. Three floats (f7940, f7944, f7945) failed early in the deployment.

An overview of float profiles and periods of operation can be found in table 3.1 (data accessible at https://data.gulfresearchinitiative.org). In total, the 10-float fleet measured over 2500 profiles over the course of the entire deployment. Of those profiles, over 1600 were recorded during continuous-mode sampling.

3.2 Sensor Calibration and Processing

3.2.1 Temperature and Salinity

At each deployment station, a CTD cast was performed using a SeaBird SBE 9 CTD. The shipboard CTD allowed for comparison between the ship measurements and the first profile recorded by the floats. At each station, a cast to 2000 m or as deep as the bathymetry at that station would allow was performed. For two float deployments, the shipboard CTD could not be deployed due to rough sea conditions. In general, the CTD and float profiles agreed very well, with an average Root Mean Square Difference (RMSD) of 0.16 °C and 0.02 psu ($N = 8$) for temperature and salinity respectively. The floats slightly underestimated

temperature and salinity with biases of –0.12 °C and –0.01 psu, respectively (Table 3.1). Information on calibration of the shipboard CTD is not known and so no adjustment of the float temperature or salinity data was performed.

Table 3.1: Float number, total number of profiles measured by each float (and subset of profiles measured in continuous mode), data of first and last transmitted profile, and RMSD and bias of temperature (°C) and salinity (psu) measurements relative to ship CTD.

Float	N_{prof} (N_{cont})	Start Date	End Date	T_{RMSD}	T_{bias}	S_{RMSD}	S_{bias}
f7939	302 (194)	02-05-2017	29-05-2018	0.17	-0.13	0.020	-0.005
f7940	83 (64)	02-05-2017	24-05-2017	0.14	-0.10	0.016	-0.009
f7941	415 (189)	03-05-2017	29-05-2018	-	-	-	-
f7942	481 (384)	03-05-2017	02-06-2018	0.15	-0.11	0.018	-0.008
f7943	384 (269)	03-05-2017	05-03-2018	0.16	-0.10	0.016	-0.002
f7944	70 (55)	03-05-2017	19-05-2017	0.17	-0.13	0.026	-0.013
f7945	186 (55)	04-05-2017	30-05-2017	-	-	-	-
f8081	322 (206)	06-05-2017	30-05-2018	0.11	-0.10	0.015	-0.011
f8082	101 (28)	06-05-2017	18-08-2017	0.15	-0.12	0.023	-0.017
f8083	312 (213)	07-05-2017	31-10-2017	0.21	-0.16	0.031	-0.023

3.2.2 Chlorophyll

Following standard Argo procedure (*Schmechtig et al.*, 2015), raw fluorescence counts (unitless) recorded by the sensor were converted to chlorophyll concentration (mg m^{-3}) by multiplication by the gain after the subtraction of the dark count of the sensor:

$$chl_a = m(fluo - dark) \tag{3.1}$$

The gain and dark count were provided by the manufacturer, however the dark count was updated to be the median of the minimum fluorescence measurements taken below 900 dbar by the float on its first 5 profiles. Although the gain (m in eq. 3.1) is known to change based on community species composition, nutrient status, light levels, depth, or season (*Roesler and Barnard*, 2013; *Roesler et al.*, 2017), the factory conversion was not altered as no independent measurements were available to make these kind of changes.

Non-photochemical Quenching (NPQ) was not corrected for, as the correction used by the Argo program described in *Xing et al.* (2012) can overestimate chlorophyll concentration at the surface in waters where the depth of the Deep Chlorophyll Maximum

(DCM) maximum and the Mixed Layer Depth (MLD) are comparable. The Gulf of Mexico displays a consistent DCM through all seasons that sometimes lies near the base of the mixed layer. When the correction would be appropriate, i.e. when the MLD and DCM are not co-incident, the NPQ correction would be very small or not change surface chlorophyll at all, as concentrations above the DCM are uniform and quite low. At other times the correction would overestimate the true surface concentration (see Figure 3.4). Profiles taken during the day and night were compared and surface concentrations were not appreciably different between the two, also indicating that there was not significant NPQ.

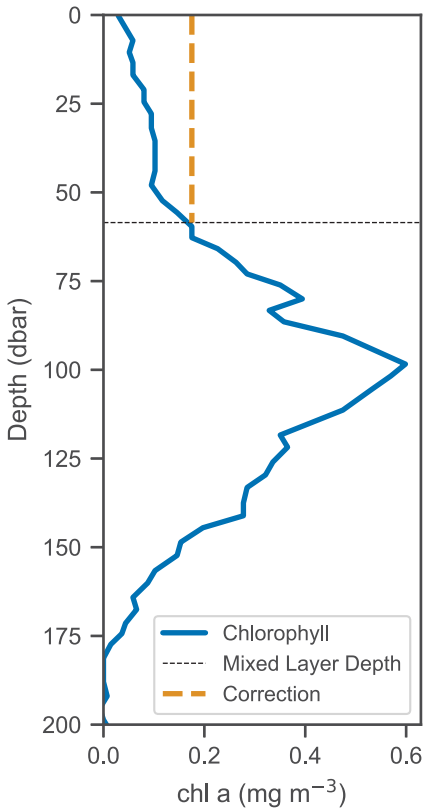

Figure 3.4: The MLD (black dashed line) often encroaches on the DCM. The correction for NPQ (orange dashed line) following the method in *Xing et al.* (2012) would create an overestimate of surface chlorophyll. Since surface concentrations are generally low in this region and the effect of quenching on the profiles is small, no correction for NPQ is performed.

3.2.3 Particulate Backscattering

Backscattering was derived from the sensor measurement following Biogeochemical (BGC)-Argo procedures for processing backscatter (*Schmechtig et al.*, 2018). Counts from the sensor (unitless) are converted to the Volume Scattering Function (VSF) at the sensor measurement angle using a factory-provided gain (in m^{-1} sr^{-1}) and a dark count:

$$\beta = m(counts - dark) \tag{3.2}$$

Seawater will also scatter light, so the VSF for pure seawater is calculated using temperature and salinity (*Zhang et al.*, 2009), and subtracted from the sensor output:

$$\Delta\beta = \beta(\lambda) - \beta_{sw}(\lambda) \tag{3.3}$$

where each of the above quantities also depends on the wavelength (λ) of light used by the sensor to make the measurement, 700 nm in this case. The resulting difference (attributed only to particles and not seawater) is multiplied by a scale factor χ (eq. 3.4) determined by the wavelength and solid angle of the sensor ($\Omega = 2.3\,\mathrm{sr}$), giving b_{bp} in m^{-1}:

$$b_{bp} = 2\pi\chi(\lambda, \Omega)\Delta\beta \tag{3.4}$$

Spikes in backscatter are representative of sinking aggregates of organic matter. Profiles can be separated into a baseline and spike components (*Briggs et al.*, 2011, Figure 3.5). When using backscatter as a proxy for suspended biomass, the baseline component of the profile was used with aggregate spikes removed.

3.2.4 Dissolved Oxygen

Oxygen was derived from the optode sensor (Aanderaa 4330, see Figure 3.6) which functions by emitting blue light on an oxygen-sensitive foil and measuring the phase difference between incident and returned light (*Kautsky*, 1939). Sensors also include a red LED which will not be shifted by the sensing foil and is used as a blank to evaluate sensor drift over time. The sensing foil is subject to boundary layer effects that lead to a

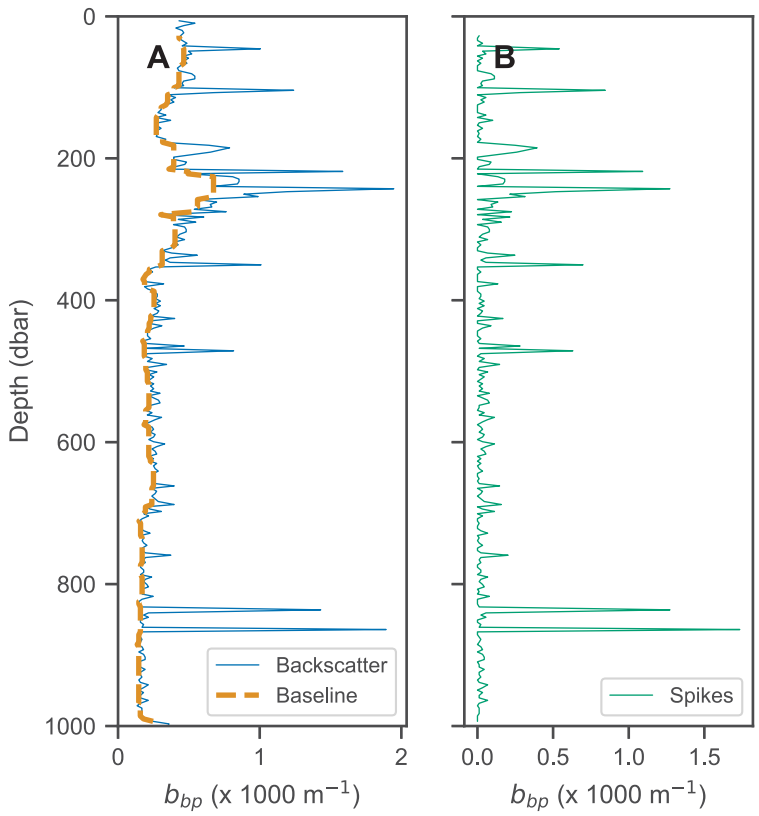

Figure 3.5: Example profile of particulate backscatter (b_{bp}) showing the separation of the profile into (A) baseline (orange dashed line) and (B) spike components following *Briggs et al.* (2011).

slow sensor response time, for which the correction will be discussed in depth. Sensor phase measurements were converted to dissolved oxygen concentration following the procedure outlined in the Argo manual for processing oxygen (*Thierry et al.*, 2016), using seven manufacturer-provided constants derived from a multi-point calibration. Salinity compensation and pressure effects are corrected for in the conversion process as well following *Bittig et al.* (2015).

Oxygen data is corrected based on an in-air measurement as well. The oxygen optode is located on a 10 cm stalk on the top of the float so that it may record a measurement of atmospheric oxygen each time the float surfaces to transmit data. The correction is made following the method outlined in *Johnson et al.* (2015). In brief, the float in-air measurement is compared to known atmospheric oxygen calculated using National Centers for Environmental Protection (NCEP) reanalysis air pressure at 10 m above sea-level and the molar fraction of oxygen in air (X_{O_2}, unitless), and a multiplicative factor (gain,

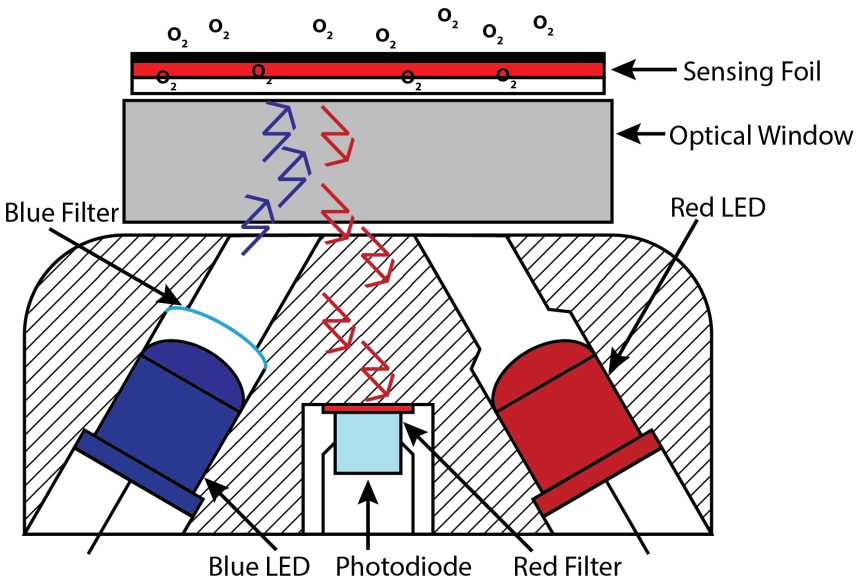

Figure 3.6: Schematic view of oxygen sensor adapted from *Tengberg et al.* (2006). Light from the blue LED is phase-shifted by the oxygen sensitive sensing foil, and the resulting shifted light is measured by the photodiode. The measured phase shift of the light is proportional to the ambient oxygen concentration. The read LED does not experience the same phase shift and can be used as a blank measurement to quantify sensor drift.

unitless) is applied to the sensor oxygen to match it to the true atmospheric value:

$$g_i = \frac{\mathrm{pO_2}}{\mathrm{pO_{2\ optode}}} \tag{3.5}$$

$$\mathrm{pO_2} = (P_{NCEP} - \mathrm{pH_2O}) \times X_{O_2} \tag{3.6}$$

Where g_i is the gain for a single in-air measurement, $\mathrm{pO_2}$ is the partial pressure of oxygen calculated using NCEP reanalysis pressure, and $\mathrm{pH_2O}$, the vapor pressure of water measured by the sensor, and $\mathrm{pO_{2\ optode}}$ is the partial pressure measured by the optode (all pressures measured in kPa). Oxygen optodes are generally stable after deployment, although it has been shown that oxygen sensors may experience some drift over time (*Bittig and Körtzinger*, 2016; *Johnson et al.*, 2017). During the deployment, negligible drift was present as calculated gains were consistent throughout. Therefore, the mean gain G for each float was applied to all oxygen data recorded by that float:

$$G = \frac{1}{N}\sum_{i}^{N} g_i \tag{3.7}$$

$$\mathrm{O_2} = G \times \mathrm{O_2}_{\,raw} \tag{3.8}$$

A summary of gain values for each float can be found in Table 4.1.

Oxygen sensors suffer from a slow response time because ambient oxygen must diffuse first through a boundary layer that establishes at the sensor interface with ambient seawater and then through a silicone sensor foil to the impermeable interface at the optical window (see Figure 3.6), which takes some time. This problem is not unique to oxygen sensors, however they do have significantly longer response times than other sensors (such as CTDs, *Bennett and Huaide*, 1986), creating more significant errors. The sensors effective response time is a combination of a response time inherent to the sensor itself (related to the thickness of the sensor foil) and a response time due to the boundary layer which varies with boundary layer thickness. A thinner boundary layer will result in faster response times. The response time inherent to the Aanderaa optodes used on these floats is reported to be 25 s for 63% of the signal (equivalent e-folding time of 51 s). The thickness of the velocity boundary layer depends primarily on the flow speed of seawater over the sensing foil (and hence the vertical velocity of the float and ambient currents), and the molecular kinematic viscosity of water.

Methods for correcting the hysteresis in oxygen measurements that results from the response time have been established, but require knowledge of the sensors time constant (*Bittig et al.*, 2014; *Bittig and Körtzinger*, 2016; *Bittig et al.*, 2018), which is difficult to characterize in the field without a true oxygen profile to reference. To correct for sensor hysteresis, a novel method for determining the time constant in-situ is presented here. Details of the method are discussed in chapter 4.

Overall, all oxygen measurements or derived quantities have been corrected for salinity and pressure effects, calibrated to in-air measurements performed by the float, and accommodate for slow sensor response time.

3.3 Numerical Model Description

A one-dimensional (1D) numerical model, simulating the ocean only in the vertical direction (thus ignoring horizontal advection) is used in addition to the float data. The physical component of the model governs vertical turbulent diffusion of the biogeochemical and physical state variables with no-flux boundary conditions at the surface and bottom (*Lagman et al.*, 2014). The biological component of the model is an adaptation of the nitrogen-based biological model of *Fennel et al.* (2006). The model simulates the top 200 m of the water column with a vertical resolution of 0.5 m and evolves forward in time using a timestep of 15 min. Simulations were run for periods of continuous mode float operation.

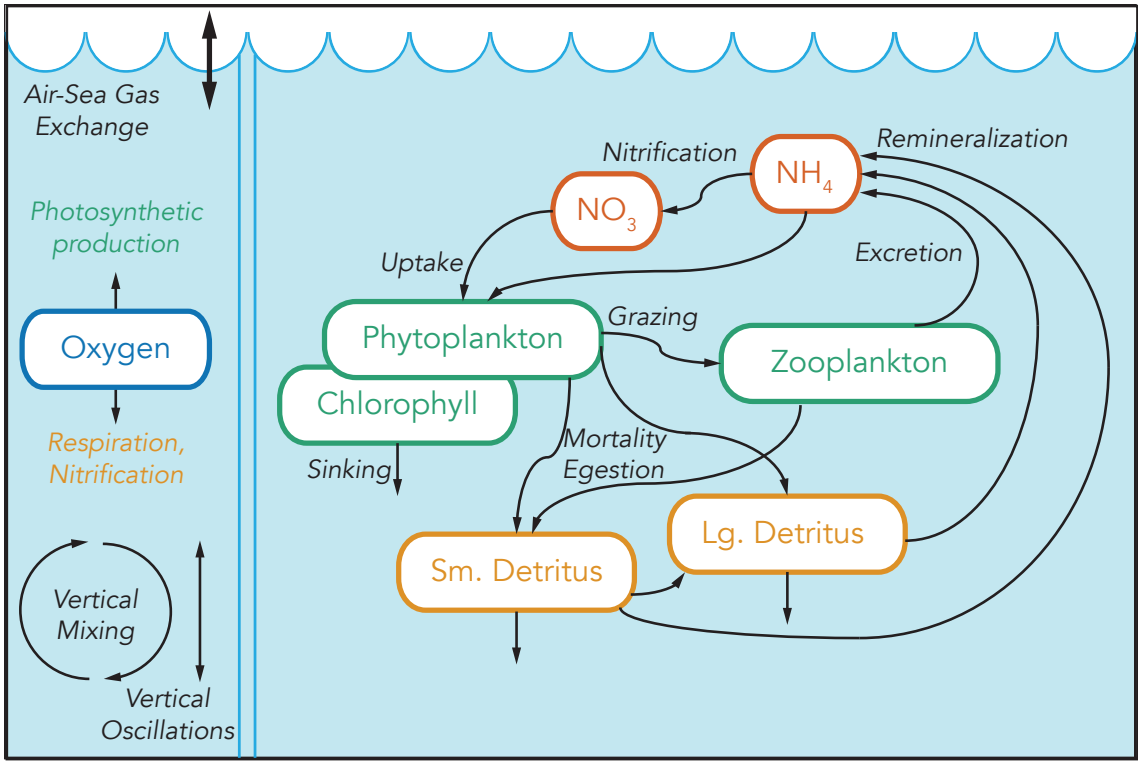

Figure 3.7: Schematic of the 1D numerical model.

The physical component of the model distinguishes two layers, the turbulent surface mixed layer (its depth is provided as model input from the float observations and is calculated by finding the first 0.5 °C temperature anomaly relative to the surface), and a quiescent layer below. In practice, this means that all grid cells in the upper layer are assigned a diffusion coefficient that ensures complete mixing on a timescale of 1 d

($k_{D1} = z_{MLD}^2$, units of d^{-1}). The diffusivity for grid cells in the lower layer was chosen to be 3 orders of magnitude smaller than the upper layer diffusivity ($k_{D2} = k_{D1} \times 10^{-3}$) following *Kuhn et al.* (2015). The Crank-Nicolson scheme was used to integrate the diffusion equation at each timestep. The mixed layer depth for the model is determined using float measurements, and then interpolated to match the models temporal resolution.

The biogeochemical component of the model consists of eight state variables: phytoplankton, Phy, zooplankton, Zoo, nitrate, NO_3, ammonium, NH_4, small and large detritus, $SDet$ and $LDet$, phytoplankton chlorophyll Chl, and dissolved oxygen O_2. The biological variables are in units of nitrogen (mmol N m^{-3}) with the exception of chlorophyll (mg Chl m^{-3}) and oxygen (mmol O_2 m^{-3}). Temperature T (°C) and salinity S (unitless, practical salinity scale psu) are also included in the model, totalling ten state variables. All variables are subject to vertical diffusion. The general processes affecting the biological state variables are described below, and the full model equations can be found in appendix A.

All common variables between the model and floats (temperature, salinity, chlorophyll, phytoplankton via backscatter, and oxygen) were initialized in the model using float observations. Nitrate was initialized using a polynomial fit to temperature and salinity observations, established using World Ocean Atlas (WOA) data. Remaining variables (zooplankton, small and large detritus, ammonium) were initialized using data from a 3D Regional Ocean Modeling System (ROMS) simulation of the Gulf of Mexico that employs the same biogeochemical model. Model parameters were based on *Bagniewski et al.* (2011), with the exception of K_{NH_4}, τ, Θ_{max}, w_{phy}, w_{SDet}, and w_{LDet} which were re-calibrated. A list of model parameters and values can be found in table 3.2.

Phytoplankton is subject to changes due to growth through nutrient uptake, grazing by zooplankton, general mortality, aggregation with detrital material, and sinking. Growth rates are temperature dependent and may be limited by light or nutrient availability. Chlorophyll concentration is subject to all the same processes, multiplied by the ratio of chlorophyll pigment to phytoplankton biomass.

Zooplankton increases through assimilation of phytoplankton at a defined efficiency. Zooplankton loss terms include mortality proportional to the square of the zooplankton concentration that goes into the detrital pool, and excretion that goes to the ammonium pool. Small detritus receives the mortality flux of phytoplankton and zooplankton, as well

as any non-assimilated phytoplankton matter during zooplankton grazing. Aggregation of small detritus and phytoplankton feed into the large detritus pool. The organic matter concentrations in both detrital groups decrease as they are remineralized at their respective constant remineralization rates. Remineralized detritus and excretion from zooplankton feeds into the ammonium pool. The cycle is completed by nitrification of ammonium feeding into the nitrate pool.

Relevant oxygen fluxes are converted using stoichiometric ratios. Oxygen is produced during the growth of phytoplankton through photosynthesis and consumed in nitrification and remineralization processes. Oxygen also decreases with zooplankton excretion. Exchange of oxygen between seawater and the atmosphere occurs in the surface layer of the model.

An option to simulate the effect of vertical oscillations of isopycnals on the biological tracers was implemented in order to study how such a physical process may affect the diurnal dynamics of oxygen production and the capacity of profiling floats to measure this signal.

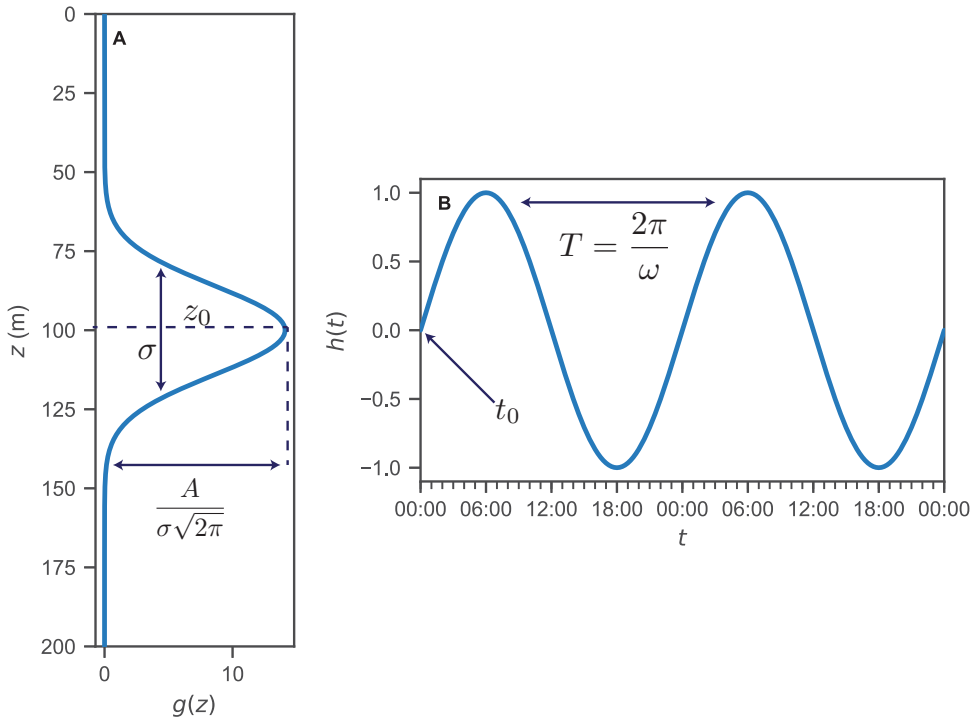

Figure 3.8: Spatial-temporal behaviour of the vertical velocity with annotated parameters showing what properties they control in (A) vertical and (B) temporal contexts.

Table 3.2: Model parameters.

Symbol	Parameter	Value	Unit
μ_{max}	maximum phytoplankton growth rate	1.0	d^{-1}
k_{NO_3}	half-saturation concentrationfor uptake of NO_3	2.0	mmol N m^{-3}
k_{NH_4}	half-saturation concentrationfor uptake of NH_4	88	mmol N m^{-3}
α	initial slope of the P-I curve	0.125	mol C (g Chl)$^{-1}$ (W m^{-2})$^{-1}$ d^{-1}
g_{max}	maximum grazing rate	0.75	(mmol N m^{-3})$^{-1}$ d^{-1}
k_P	half-saturation concentration of phytoplankton ingestion	0.5	(mmol N m^{-3})^2
m_P	phytoplankton mortality	0.01	d^{-1}
τ	aggregation parameter	0.41	(mmol N m^{-3})$^{-1}$ d^{-1}
Θ_{max}	maximum chlorophyll to carbon ratio	0.0208	mg Chl (mg C)$^{-1}$
β	assimilation efficiency	0.75	dimensionless
l_{BM}	excretion rate due to basal metabolism	0.01	d^{-1}
l_E	maximum rate of assimilation related excretion	0.1	d^{-1}
m_z	zooplankton mortality	0.2	(mmol N m^{-3})$^{-1}$ d^{-1}
r_{SD}	remineralization rate of small detritus	0.3	d^{-1}
r_{LD}	remineralization rate of large detritus	0.25	d^{-1}
n_{max}	maximum nitrification rate	0.2	d^{-1}
k_I	light intensity at which the inhibition ofnitrification is half-saturated	0.1	W m^{-2}
I_0	threshold for light-inhibition of nitrification	0.0095	W m^{-2}
w_{phy}	sinking velocity of phytoplankton	0.009	m d^{-1}
w_{SDet}	sinking velocity of small detritus	0.341	m d^{-1}
w_{LDet}	sinking velocity of large detritus	3.41	m d^{-1}
$R_{O_2:NO_3}$	ratio of O_2 to NO_3	8.625	mol O_2 (mol N)$^{-1}$
$R_{O_2:NH_4}$	ratio of O_2 to NH_4	6.625	mol O_2 (mol N)$^{-1}$

Vertical oscillations are simulated by a space (z) and time (t) dependent vertical velocity, w (m d^{-1}), which is included in all tracer equations in the following form:

$$\frac{\partial C}{\partial t} = \ldots - w(z,t)\frac{\partial C}{\partial z} \tag{3.9}$$

where C is the concentration of any tracer in the model.

This vertical velocity (equations 3.10a-3.10c) is defined by a Gaussian function in the vertical direction and a sinusoidal wave in time (Figure 3.8) dependent on 5 parameters. The parameters are Gaussian amplitude coefficient (A, m^2 d^{-1}), width (σ, m), and central depth (z_0, m) of the vertical Gaussian distribution, and the frequency (ω, d^{-1}) and initial state of the sinewave determined by t_0 (d). Defined in this way, vertical oscillations that are simulated at a depth of $z_0 = 100\,\mathrm{m}$ do not influence the upper and lower boundaries of the vertical grid. In Figure 3.8, water near the peak of the vertical Gaussian distribution will be displaced about 10 m, while water near 120 m will only move about half that distance. This creates highly localized vertical displacements around the oxygen gradient.

The vertical velocity is expressed as the product of a Gaussian profile in space and a sinewave in time:

$$w(z,t) = g(z)h(t) \tag{3.10a}$$

$$g(z) = A\frac{1}{\sigma\sqrt{2\pi}}\exp\Big(-\frac{1}{2}((z-z_0)/\sigma)^2\Big) \tag{3.10b}$$

$$h(t) = \sin(\omega(t-t_0)) \tag{3.10c}$$

Introducing vertical velocities into the model implies, by the continuity eqiation, that there must be non-zero horizontal velocities $u(x,z,t)$ and $v(y,z,t)$. These velocities are clearly not possible to include in the 1D vertical-only model, however as we work under the assumtion that all tracers are uniform in the horizontal, they can be ignored without introducing error into the results. That is, we assume that for the concentration of a given tracer C:

$$\frac{\partial C}{\partial x} = \frac{\partial C}{\partial y} = 0 \tag{3.11}$$

Using the 1D model, three different model experiments (Model Experiments (ME)s) are conducted. The first, ME1, is to examine how the slow response time of the oxygen optode and subsequent corrections may introduce error into the data. The second, ME2, is to assess the feasibility of measuring the biologically driven diurnal oxygen cycle for various sampling schemes and magnitudes of measurement error. In the third and final experiment, ME3, assesses the impact of vertical oscillations of the water column.

Table 3.3: Summary of model experiments (ME).

Experiment	**Objective**
ME1 – No biological activity	Examine how the oxygen optode observes an oxygen profile, and how the correction of sensor hysteresis induces or affects existing error in the measurement.
ME2 – Biological model, no vertical oscillations	Evaluate how well the diel cycle would be observed for different sampling schemes and/or measurement errors
ME3 – Biological model and vertical oscillations	Characterize the interaction of the biologically driven diel oxygen cycle and vertical oscillations.

Each experiment required a different model setup or treatment of model output as summarized in Table 3.3, and discussed in greater detail throughout chapters 4 and 5.

CHAPTER 4

RESPONSE TIME CORRECTION METHOD

4.1 Sensor Hysteresis Correction

A typical set of oxygen profiles from consecutive up- and down-casts shown in Figure 4.1 illustrates a discrepancy in the oxycline that is generally found between two consecutive casts. This is due to the slow response time of the oxygen sensor causing hysteresis, which is especially pronounced when measuring steep oxygen gradients. During the up-cast, the oxygen gradient appears shallower than in reality, and vice-versa during the down-cast. The true oxygen gradient must lie in between the two profiles. Working under the assumption that oxygen does not significantly change between consecutive profiles during continuous sampling (the top 200 m of adjacent profiles were separated on average by about 70 min), the availability of up- and down-casts offers an opportunity to estimate the effective response time *in-situ*.

In order to estimate response time and perform correction on the oxygen profiles, one must first understand the mechanism causing the error. The observation of an oxygen profile by an optode can be described by the following differential equation:

$$h(t) = f(t) - \tau \frac{\partial h}{\partial t} \tag{4.1}$$

where $h(t)$ is the oxygen concentration at time t measured by the optode (mmol O_2 m^{-3}), $f(t)$ is the true ambient oxygen concentration (mmol O_2 m^{-3}), and τ is the effective response time (s) determined by the sensor and environment.

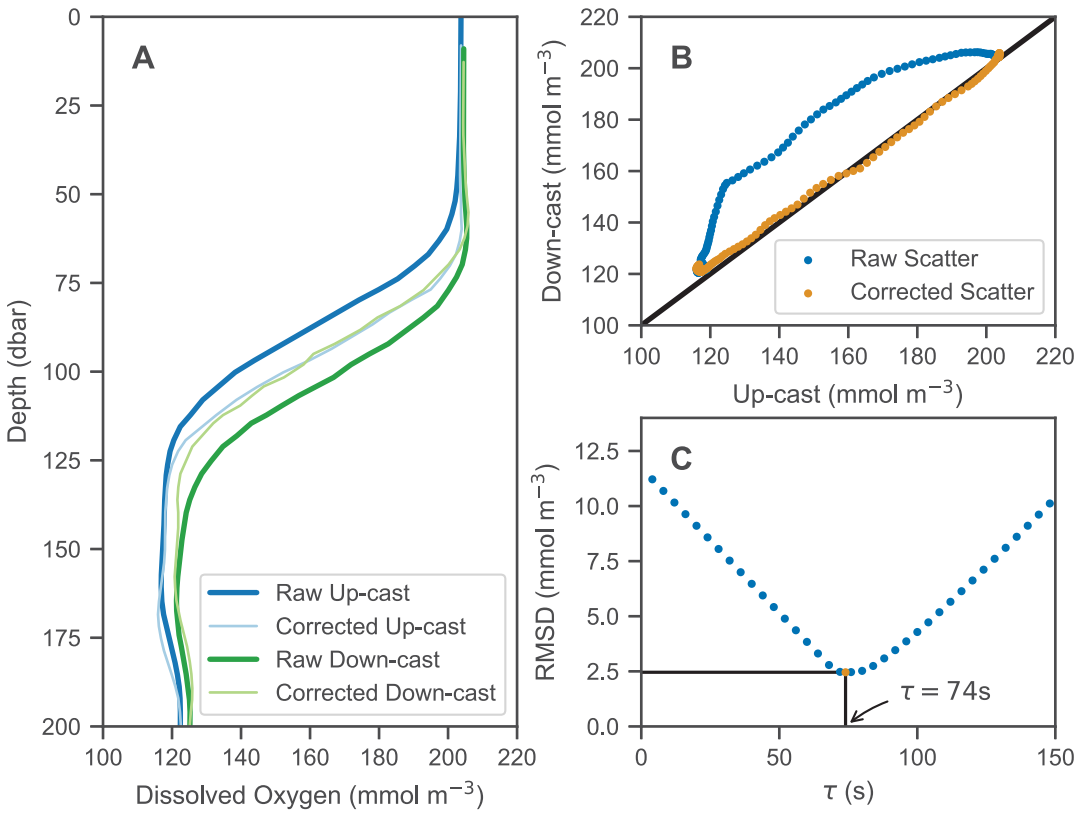

Figure 4.1: Example of method for determination of sensor time constant. (A) Darker, thicker lines show raw measurement of up- (blue) and down- (green) casts. The up-cast has a memory of the low concentration in deep water and measures the gradient to be shallower than its true position, and the reverse is true for the down-cast. Lighter, thinner lines show the corrected profiles. (B) Scatter of raw (blue points) and corrected (orange points) up- and down-casts between 50-150 m. (C) The RMSD between the up- and down-casts for each time constant, showing the optimal τ value in this case of 74 s.

This differential equation can be solved using a Laplace transform, and a full derivation is provided in appendix B. The resulting solution is written as:

$$h(t) = f(0)\mathrm{e}^{-t/\tau} + \frac{1}{\tau}\int_0^t f(t-u)\mathrm{e}^{-u/\tau}du \tag{4.2}$$

The first term of equation 4.2 represents the decaying initial condition of the sensor, where we have assumed that at time $t = 0$, the sensor reads the correct, true oxygen concentration (i.e. $h(0) = f(0)$). The second term is the convolution (definition from *Boas*, 2006, pg. 444) of the true oxygen concentration and a decaying exponential which represents the

transfer function of the sensor.

Thererfore, the observations h could be more generally expressed as:

$$h = f * g \tag{4.3}$$

where h represents the measurement, f is the true concentration, and g is the function representing the response of the sensor (unitless). To recover the correct oxygen profile, we must perform the *deconvolution* of the profile and the sensor. This is a difficult but possible task if the observations h are known (and have timestamps), and the equation describing the sensor transfer function g is known. From equation 4.2 sensors transfer function can be defined as:

$$g(t) = \frac{1}{\tau}\mathrm{e}^{-t/\tau} \tag{4.4}$$

This provides the mathematical basis for correcting the sensor hysteresis.

Equation 4.4 is the impulse response of the sensor's output when measuring step change in oxygen (subsequently referred to as step-response, see Figure 4.2A). A step response is typically written as:

$$y(t) = 1 - \mathrm{e}^{-t/\tau} \tag{4.5}$$

Meaning that for a given change in oxygen concentration during the profile, the sensor will approach the new oxygen concentration at a rate proportional to the response time τ.

Taking the Laplace transform of the impulse response in equation 4.4 and assigning the proper Laplace variable s, one can recognize that this is a single-pole low-pass filter. To this point, the sensor theory has been discussed in continuous time. In order to apply a correction to the data, it must be in the discrete time domain. By discretizing the Laplace transform using a *bilinear transformation* and then performing the inverse discrete Laplace transform (or *Z-transform*, see *Proakis and Monolakis*, 1996; *Antoniou*, 2018) on the result, we derive the following relationship:

$$h_n = ah_{n-1} + b(f_n + f_{n-1}),\ n = 1, \ldots, N \tag{4.6}$$

where:

$$b = \left(1 + 2\frac{\tau}{t_n - t_{n-1}}\right)^{-1},\ a = 1 - 2b \tag{4.7}$$

with a and b both being unitless coefficients.

The above equations can be re-written in the same form as provided by *Bittig and Körtzinger* (2016), eq. A3:

$$\frac{f_n + f_{n-1}}{2} = \frac{1}{2b}(h_n - ah_{n-1}) \tag{4.8}$$

Deconvolution is a difficult task in that it is known to amplify errors in systems such as this one where the truth $f(t)$ is convolved with the transfer function of an instrument $g(t)$. Equation 4.3 is more appropriately written as:

$$h = f * g + \epsilon \tag{4.9}$$

where ϵ is random noise.

Depending on the signal-to-noise ratio, inverse filtering techniques like the one described above may provide inaccurate estimations of the truth $f(t)$. With knowledge of the nature of the error ϵ, smoothing or filtering techniques may improve the final estimate (*Wiener*, 1964).

Although timestamps are often not transmitted from profiling floats, all data recorded by our floats had timestamps with each measurement. Next, a method for determining the sensors effective time constant in-situ is described.

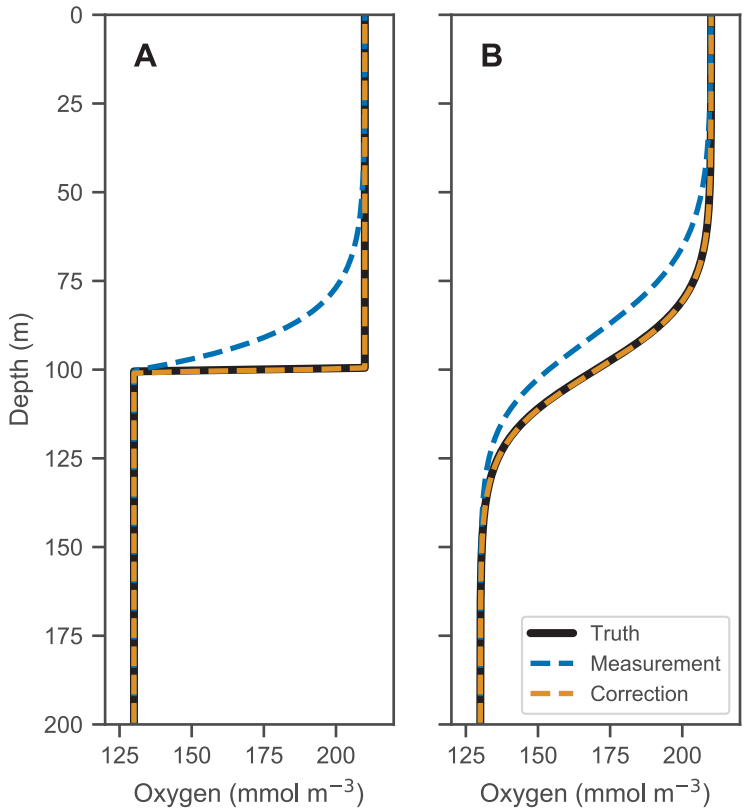

Figure 4.2: Examples of idealized profiles (black lines), up-cast measurements of these profiles with a time constant τ of 75 s (dashed blue lines) and corrected profiles (orange dashed lines) (A) a step function and (B) an idealized profile similar in magnitude to those observed in the Gulf of Mexico.

4.2 Determination of Sensor Time Constant

Determination of the effective time constant for each sensor is possible because the up- and down-casts are recorded consecutively on a short timescale. Assuming the oxygen profile has not substantially changed in the one hour between up- and down-cast, the two casts should agree after correction. Timestamps were transmitted with the data, and so are available for the correction.

The low-pass inversion, while correcting the hysteresis resulting from the slow response time, may have the undesired effect of amplifying high- frequency noise. To mitigate this, I have chosen to smooth profiles using a 7-pt moving mean prior to performing the correction (figure 4.3).

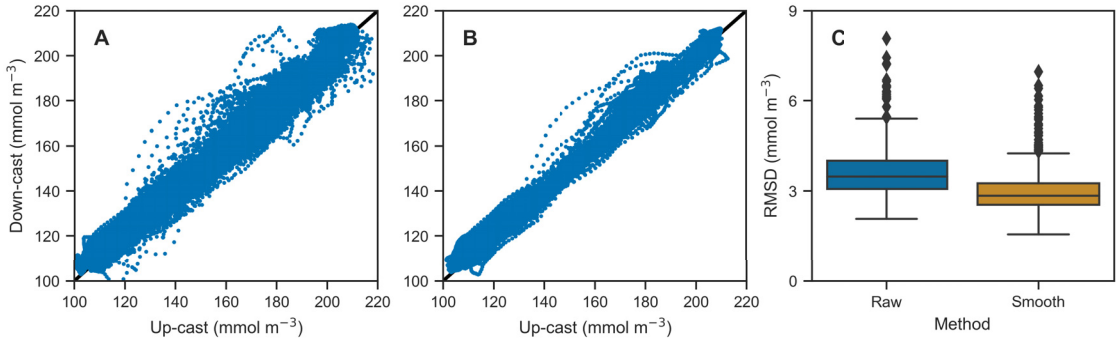

Figure 4.3: Scatter of up- vs. down-casts for (A) unsmoothed and (B) smoothed profiles, both after correction and (C) a Tukey boxplot of the RMSD in each case – showing that the smoothed profiles have a lower median (middle line of box) RMSD. The outer edges of the boxes represent the first and third quartiles of the data, the extent of the whiskers shows the lowest and highest data within the 1.5 interquartile range, and points show outliers.

Smoothing the profiles was important to a successful correction of sensor hysteresis due to the response time, as the inverse filter amplifies random errors. This was particularly true for the down-cast measurements. Profiling floats typically only measure on the up-cast because most of the sensors are located near or at the top of the float, and so recording on the up-casts allows the sensors to measure quiescent, undisturbed water. When measuring on the down-cast, water has been churned up by the body of the float, and so the down-casts for oxygen (and other variables) may have increased random errors. Smoothed profiles agreed much more closely in the oxygen gradient, and the RMSD was generally lower in smoothed profiles after correction (Figure 4.3). Some anomalous pairs of profiles still disagreed in a significant way; this disagreement however was not attributed to the correction process.

An illustration of the process for determining the time constant is shown in Figure 4.1; also shown is the effect of the hysteresis correction on the profiles (panel A, thin lines). Determination of the effective response time is done by systematically sweeping over the range of possible response times from 0 to 150 seconds on 0.5 s increments and applying the response time correction following *Bittig and Körtzinger* (2016) and eq. (4.8) for each. RMSD between the up- and down-casts for each response time value is calculated (Figure 4.1C) and the time constant with the minimum RMSD is taken to be the effective time constant for that pair of profiles.

This calculation is done for each pair of consecutive up- and down-casts and down- and

up-casts, resulting in a population of $N-1$ effective time constants for each set of N float profiles. The median time constants for each float are listen in Table 4.1. Median optimal time constants ranged from 64.5-76.5 s across the 10 floats, and the standard deviation of those values was as low as 8.5 s and as high as 20.4 s.

Table 4.1: Gain values applied to each float with standard deviation, and time constants applied to each float with standard deviation.

Float	G (unitless)	σ_G (unitless)	μ_τ (s)	σ_τ (s)
f7939	1.17	0.18	76.5	8.5
f7940	1.03	0.12	69	15.5
f7941	1.14	0.17	67	16.9
f7942	1.17	0.24	64.5	14.9
f7943	1.15	0.19	75	16.5
f7944	1.15	0.12	76	13.9
f7945	1.16	0.14	73.5	13.3
f8081	1.18	0.20	68	16.0
f8082	1.15	0.09	73	18.8
f8083	1.12	0.18	66.5	20.4

Similar to the gain correction where the mean gain calculated by in-air measurements is applied to all data for that float (see Methods Section 3.2.4), I chose to apply the median optimal response time of each float to all profiles from that float.

The variation of effective response time from profile to profile for the same float is due to its dependence on various factors that affect the effective response time, chiefly among them is the flow speed of ambient water over the sensor. Next, I analyze how deviations from the average profiling speed and random errors manifest themselves in the final corrected oxygen product.

4.3 Propagation of Response-time Error and Sensor Noise

Oxygen measurements made by autonomous floats are subject to systematic and random sources of error. First, the effective response time may change with variations in temperature, salinity, pressure, and most importantly flow speed of ambient sea water at the sensing interface; the latter is highly dependent on profiling velocity. Profiling velocity ideally should be constant but varies in practice (1.4-26.5 cm s^{-1} with a mean value of

12.2 cm s^{-1} for our floats). It is important to characterize how errors resulting from these variations propagate through the response-time correction. Second, random error present in the observation made by the sensor will propagate through the correction process. This random error may be amplified by the response time correction.

The goal of the first model experiment, ME1, is to simulate how these two different errors affect the measured profile and to what degree they may compromise our ability to derive the true profile from the measurements. For this purpose, the model output is sampled similar to a float profiling in continuous mode, with a profiling velocity of 15 cm s^{-1} and a measurement every 5 m. The response time effect is simulated by applying a discretized version of equation (eq. 4.1):

$$\begin{aligned} &h_n = \alpha f_n + (1-\alpha) h_{n-1} \\ &\text{where: } \alpha = \frac{\Delta t}{\tau + \Delta t},\ h(0) = f(0) \end{aligned} \tag{4.10}$$

where h_n and f_n are the the filter output (measurement) and input (true ambient oxygen concentration) at timestep n respectively. The term on the right hand side of equation 4.10 including f_n represents the real-time contribution to the measurement, and the term including h_{n-1} represents the sensors inertia or memory of previous measurements. A full derivation of this discretized form is given in appendix B. The recursive structure of the filter results in an exponentially weighted moving average, with an infinite averaging window in time.

In ME1, the generation of optode measurements is simulated by prescribing a float profiling velocity, sampling the models oxygen profile according to that velocity, assigning a timestamp to each oxygen datum, and then running the model output through the filter using a prescribed effective response time. In this model experiment, sampling is simulated for upcasts only. The results are equally applicable to downcasts, so long as the directionality of the response-time error is considered.

Known errors are inserted into this measurement process as random perturbations of the response time and as random noise added to the filtered oxygen values. The two error sources are examined individually, i.e. the analysis of the response time error will have zero sensor noise, and vice-versa. In each case, the added errors are random values drawn from a normal distribution with increasing standard deviations to systematically analyze the effect of each error type. For the response time error, response times (τ, s) are chosen

from a normal distribution with a mean value μ_τ of 75 s and standard deviations ranging from 0 to 15 s (Figure 4.4A):

$$\tau \sim N(\mu_\tau = 75, \sigma_\tau^2) \quad \sigma_\tau \in (0, 15) \tag{4.11}$$

Sensor noise errors (ϵ, mmol m^{-3}) are chosen from a normal distribution with mean of zero and standard deviations ranging from 0 to 1.5 mmol m^{-3} (Figure 4.4B):

$$\epsilon \sim N(0, \sigma_\epsilon^2), \quad \sigma_\epsilon \in (0, 1.5) \tag{4.12}$$

Therefore, the profile observation can be written as:

$$h_{obs}(t) = h(t) + \epsilon(t) \tag{4.13}$$

where $h_{obs}(t)$ is the noisy observation, $h(t)$ is the filtered true profile simulating sensor response time, and $\epsilon(t)$ is the error at each time/depth level.

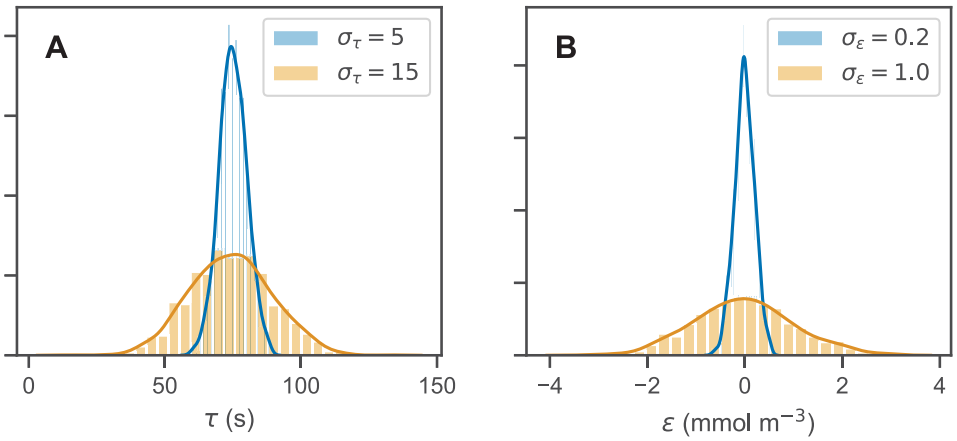

Figure 4.4: Example distributions for (A) response times with a mean of 75 s with standard deviations 5 s (blue curve) and 15 s (orange curve) (B) signal noise with standard deviations 0.2 mmol m^{-3} (blue curve) and 1.0 mmol m^{-3} (orange curve).

Following the simulated measurement, the measured profiles undergo the same correction process as the float data first using 7-pt smoothing and then running the response time correction. Different magnitudes of errors are tested and for each trial, the measurement and correction process is repeated 50 times to establish a population of simulated observations.

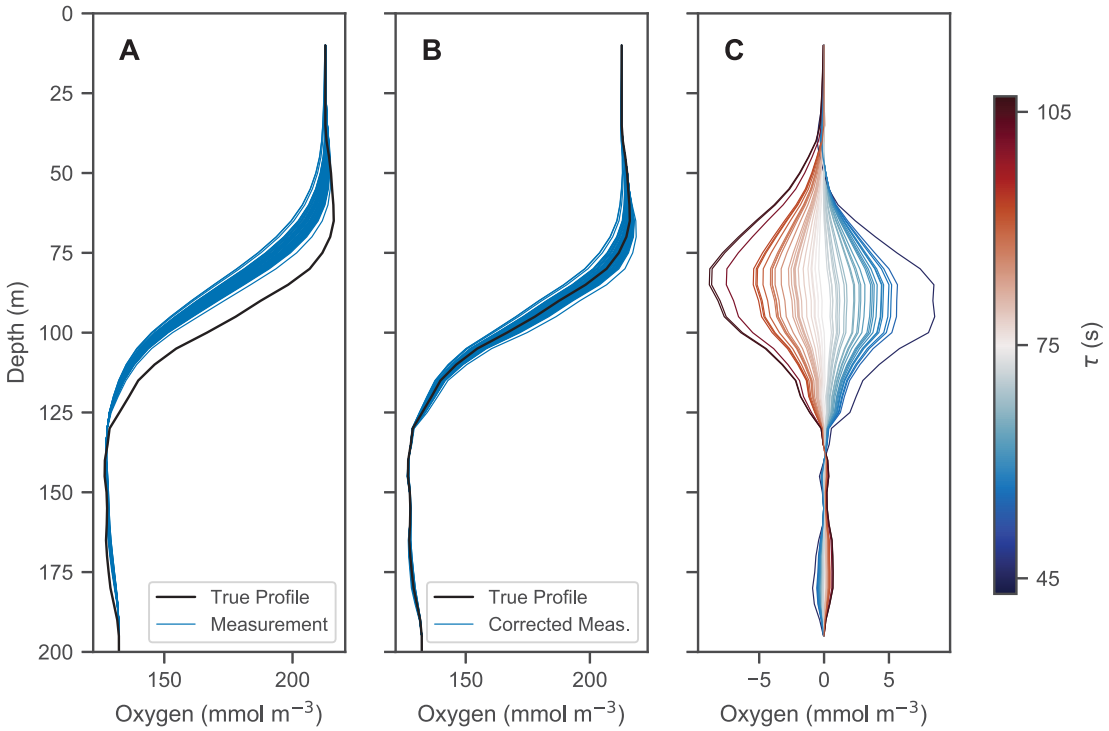

Figure 4.5: Response time error measurements, corrections, and deviations. (A) Simulated profile measurements (blue) of the true oxygen profile (black) for 50 different response times drawn randomly from a normal distribution with standard deviation of 15 s and mean of 75 s. (B) Correction of the measurements in panel (A) using a response time of 75 s. (C) Deviations of the corrected profiles from the truth.

The response time error is analyzed by randomly choosing the response time for the simulated observation from the distribution, and performing the correction using the expected value ($E(\tau) = \mu_\tau = 75\,\mathrm{s}$). Figure 4.5 shows the measurement (A) and correction (B) for the widest distribution of response times tested ($\sigma_\tau = 15\,\mathrm{s}$), in the absence of any sensor error. Despite the large error magnitude, the correction method still works relatively well. In uniform segments of the oxygen profile, the mismatch between measured and corrected response time has little to no effect in recovering the correct oxygen concentration, while larger deviations from the true profile are observed in the high gradient segments of

the profile, with a maximum deviation of almost 10 mmol m^{-3}. The deviations in Figure 4.5C are ordered by the effect of smaller or larger response times. The largest positive deviations correspond to smaller response time values chosen from the distribution ($\tau < \mu_\tau$). The negative deviations that are largest in magnitude belong to chosen response times that are largest ($\tau > \mu_\tau$). Small deviations correspond to values chosen close to the mean values ($\tau \approx \mu_\tau$).

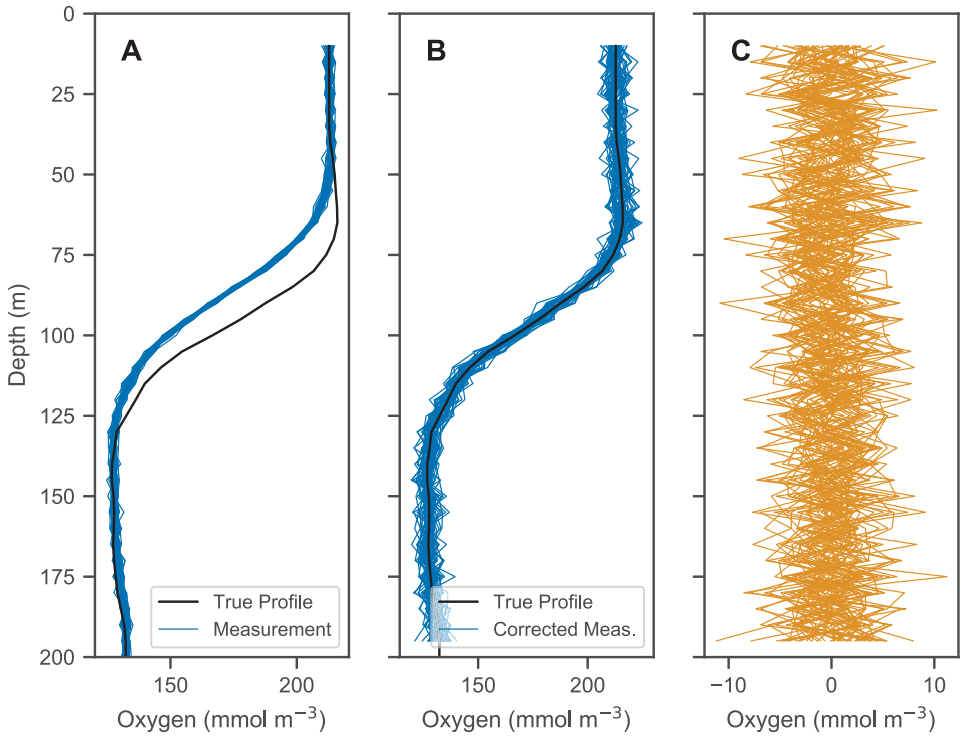

Figure 4.6: Random sensor error measurements, corrections, and deviations. (A) Measurements with Gaussian noise with a standard deviation of 1.0 mmol m^{-3} added (blue) made with a sensor response time of 75 s of the true oxygen profile (black). (B) Corrected measurements. (C) Deviations of the corrected profiles from the truth.

Next, I analyze the effect of random errors in the oxygen measurement. Simulated measurement, correction, and deviation from the true profile are shown in Figure 4.6 for an error distribution with a standard deviation of 1.0 mmol m^{-3}. In contrast to the response time error, random sensor error does not have a localized effect on the profile. Examining the measurement (blue lines in Figure 4.6A) and corrected profiles (blue lines in 4.6B), the error appears to be amplified through the correction process. This is confirmed by examining the distribution of the deviations (figures 4.5C and 4.6C).

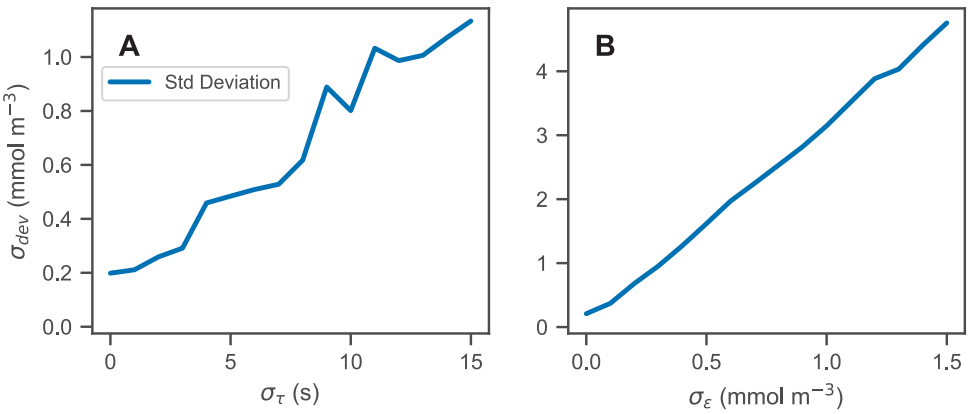

Figure 4.7: Standard deviation of the error profiles for increasingly wide distributions of (A) response time and (B) random error. For random error, σ_{dev} increases linearly with σ_ϵ, with a slope of 3.09 (unitless).

Summaries of each error analysis are shown in Figure 4.7, where the mean of the standard deviations of each deviation profile (σ_{dev}) is shown for increasingly wide distributions of response time error and random error. For response time errors, the distribution of deviations has a maximum value exceeding 1.0 mmol m^{-3}. Although large deviations up to 10 mmol m^{-3} were observed, they were highly localized to the oxygen gradient. This result demonstrates that for the correction method applied in this research, despite large ranges of response times calculated from the floats, the corrected profile is still close to the true oxygen profile. For the random noise, we see an amplification of the errors through the correction process by a factor of about 3. The standard deviation of the resulting deviation profiles, σ_{dev} increases linearly with σ_ϵ, but with a slope greater than 1. This slope is consistent with theoretical consideration (see appendix B.3).

4.4 Discussion

Oxygen optode response time is often referred to as a prominent source of error (see *Plant et al.*, 2016; *Johnson et al.*, 2017), but is not often rigorously corrected on autonomous float platforms. One reason is that the time stamps of the oxygen measurements are not typically transmitted by the float (*Johnson et al.*, 2017). Another reason is that the effective sensor response time is difficult to characterize without knowledge of the true profile against which to compare. To minimize response time errors, some optodes are pumped to significantly increase the flow speed at the interface between sensing foil and ambient

seawater and thus decrease boundary layer thickness and the effective response time. However, even pumped optodes still have a characteristic response time, albeit reduced, and have the disadvantage that they cannot record in-air measurements for calibration purposes.

Plant et al. (2016) cited response time errors as the cause of unrealistically large values of positive NCP just above the mixed layer and negative NCP below. They chose to correct mixed layer oxygen by extending surface oxygen values on the assumption that oxygen is completely uniform in the mixed layer. However, a full correction using the filtering solution provided by *Bittig et al.* (2014) could have improved NCP estimates not only at the mixed layer interface but also for the entire profile. While oxygen values near the base of the mixed layer were the most blatant evidence of error induced by the response time, any oxygen gradient would have been subject to the effects of sensor response time as well and thus would have been improved by the inverse filtering correction.

(*Johnson et al.*, 2017) compared oxygen measurements made by floats in the Southern Ocean Carbon and Climate Observations and Modelling (SOCCOM) program and Winkler titrations (*Winkler*, 1888; *Carpenter*, 1965) from bottle samples at deployment stations. While optode-measured oxygen agreed very well with the Winkler measurements, the majority of error was concentrated around high-gradient areas. Response time corrections could not be performed in this case because SOCCOM floats did not transmit time stamps for each oxygen measurements.

As previously stated, time stamps and knowledge of the sensors effective time constant are the two key pieces of information required to make a sensor hysteresis correction. In the case of the SOCCOM floats, had timing information been available, the time constant would have remained to be determined. Using the Winkler data, an analysis similar to the one done here could have been performed. However, recording consecutive up- and down-casts, at least occasionally, seems to be a much more efficient method for determining the effective response time, as demonstrated here.

The discrepancy between the effective response times derived here and sensor- inherent response times reported on the Aanderaa optode datasheet should not be surprising. While the datasheet provides an estimate of the inherent sensor response time (25 s for 67% of the signal), which is calculated by subjecting the sensor to a sudden step change by plunging from air into water, what has been determined here is the effective response time in-situ.

The effective response time also accounts for oxygen diffusing through the boundary layer at the sensing interface which is significant for typical float velocities. The $\sim 70\,\mathrm{s}$ response times found here are well aligned with previous reports of response times based on flow-dependent boundary layer thickness of 15-45 s for shipboard CTD applications (*Bittig et al.*, 2014), and 70-140 s for profiling floats (*Bittig and Körtzinger*, 2016; *Bittig et al.*, 2018). The large standard deviations of float response times (Table 4.1) are not attributable to the sensors themselves (all sensing foils for the 10 sensors came from the same batch) but more likely represent changes due to ambient physical characteristics and flow at the sensor interface. While this could represent a still significant source of error in the oxygen measurements even after applying the method described here, the improved agreement between up- and down-casts using median response times (Figure 4.3B) is encouraging.

Subjecting simulated measurements to varying effective response times and sensor error demonstrated how small deviations can have meaningful implications for the final measurement. The combined effects of these two potential sources of error caused significant deviations between the corrected measurements and true profile (Figures 4.5 and 4.6). The 50 repeated measurements of the oxygen profile with a response time error (standard deviation) of 10 s and sensor error on the order of $1.0\,\mathrm{mmol\,m^{-3}}$, resulted in deviations of approximately $1.0\,\mathrm{mmol\,m^{-3}}$ and $3\,\mathrm{mmol\,m^{-3}}$ respectively (Figure 4.7). These two relatively conservative error estimates result in a total deviation of 3-4 $\mathrm{mmol\,m^{-3}}$. This is a very significant error for the precision with which we aspire to measure cycling oxygen, and the magnitude of this deviation would be even higher in the oxygen gradient.

Bittig et al. (2018) stated that the relation between the boundary layer thickness and float profiling velocity must be established on a case-by-case basis depending on the platform characteristics and optode attachment with respect to flow direction. For this analysis, effective time response of the optode on the up- and down-casts are treated to be equal. In reality, flow around the optode may not be identical for the two cast directions (on the downcast where the optode would be measuring water disturbed by the passage of the float). However, the impact of this difference on the corrections is likely small.

My technique for determining the effective time constant is a simple and practical method for in-situ application and more straightforward than characterizing flow surrounding an optode mounted on a float. It could easily be performed by any end-user deploying a biogiochemically equipped float, as long as time stamps and occasional up- and down-casts

are transmitted.

The difference between the measured and corrected profiles is substantial. For the Gulf of Mexico, where the maximum oxygen gradient averaged 2.55 $\mathrm{mmol\,m^{-3}\,dbar^{-1}}$ for all floats, median differences between observed and correction profiles ranged from 36-39 $\mathrm{mmol\,m^{-3}}$ at the maximum gradient. Overall, we recommend transmitting timing data with oxygen measurements is a simple yet powerful change to make towards obtaining more accurate oxygen observations. In addition, we recommend a calibration period upon float deployment that records both up- and down-casts which would provide sufficient data to characterize the effective response time of the sensor, thus providing all the information required to correct for sensor hysteresis.

CHAPTER 5

BIOLOGICAL & PHYSICAL DRIVERS OF DISSOLVED OXYGEN VARIATION

5.1 Measurement of Diurnal Oxygen Cycles

Next, I attempt to estimate GOP, R, and NCP from hysteresis-corrected oxygen measurements during continuous mode profiling. This analysis can only be performed during continuous sampling because multiple measurements per day are required to resolve the diurnal signal.

In Figure 5.1, the first 8 months of data from a float f8081 are shown, including the continuous mode periods from May 2-8, September 9-20, and October 4-11. Temperature shows the expected seasonal cycle, with surface water temperatures peaking in late summer. Surface chlorophyll peaks at the beginning of September during a high-wind event (according the NCEP wind data) that precedes the passage of hurricane Irma. Elevated winds could encourage mixing and distribution of the deep chlorophyll maximum over the entire surface layer. Mean oxygen is decreasing over the observation period with some more complicated dynamics overlaid in the scatter.

5.1.1 Autonomous Measurement of Gross Oxygen Production

For biological production to occur there must be nutrients available and sufficient Photosynthetically Active Radiation (PAR). Respiration has no such constraints and will act to decrease oxygen no matter the nutrient or light conditions in the water column, so long as organic matter and respiring organisms are present. Biologically driven changes in dissolved oxygen therefore are different between day and night. During the day, oxygen

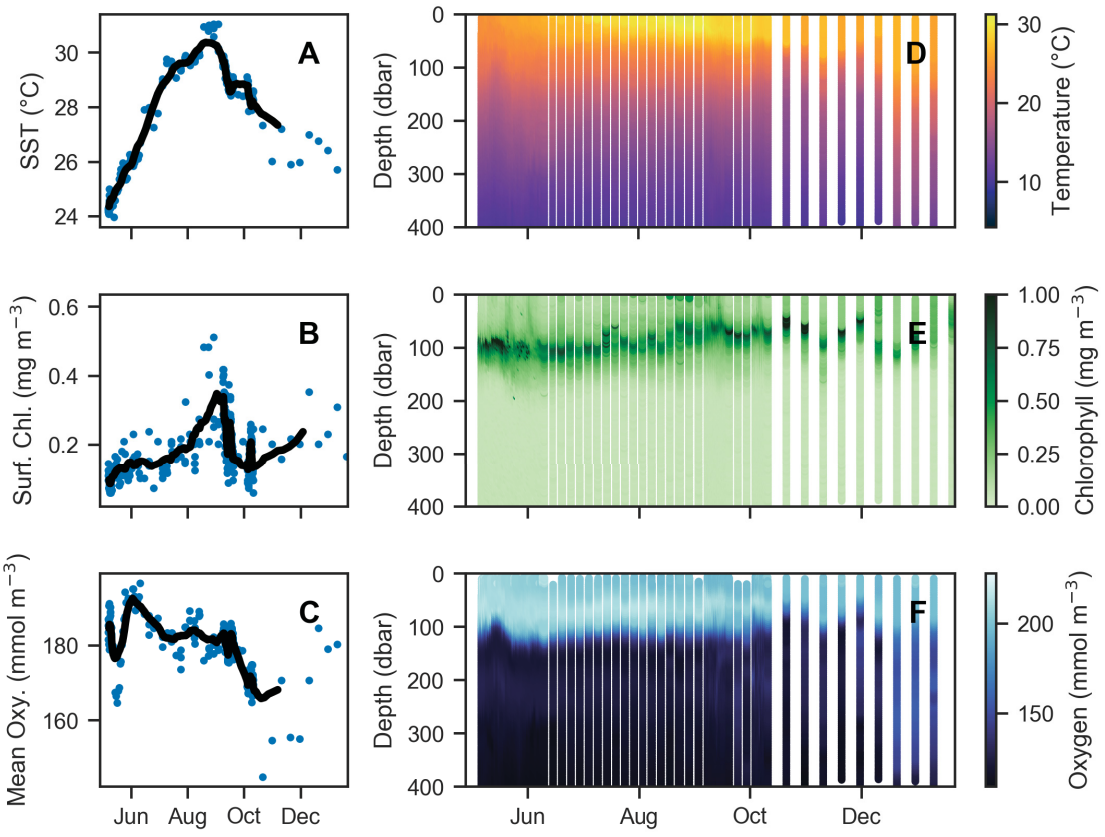

Figure 5.1: Float f8081 temperature, chlorophyll, and oxygen data. (A) Sea Surface Temperature, (B) Surface chlorophyll, and (C) Mean oxygen from 25-150 dbar observed by float f8081 from May 2017 to Jan 2018. Black lines show the 7-pt running mean. (D-F) Temperature, chlorophyll, and dissolved oxygen during the observation period. The profile density shows the periods of continuous mode measurement with more densely populated temporal data and the sparser periods of park-and-profile mode.

will change at a rate proportional to the difference between the GOP and R, and during the night, production does not occur (GOP$= 0$), but respiration continues:

$$\left.\frac{\partial O_2}{\partial t}\right|_{bio} = \begin{cases} GOP - R & \text{daytime} \\ -R & \text{nighttime} \end{cases} \tag{5.1}$$

The framework presented here assumes respiration is constant throughout the day and night, and that during daylight hours gross production is constant (GOP $=$ const.). This results in periodic signal in oxygen.

GOP can be estimated from diurnal oxygen cycles of this idealized structure, i.e. minimum oxygen near dawn, maximum near dusk. This is essentially what *Briggs et al.* (2018) assumed when they applied a linear fit to the nighttime data, where the slope represents the respiration rate, and extrapolated forward to noon the next day to project the dissolved oxygen concentration in the absence of any production (Figure 5.2, dashed lines). To obtain an estimate for morning GOP, a second linear fit was applied to the daytime data and the difference between the extrapolated nighttime fit and the value of the daytime fit at noon is the oxygen produced that morning (Figure 5.2, light green bars). The oxygen produced in the second half of the day is calculated in a similar fashion, but by extrapolating the fit of the data from the following night backward to find the oxygen concentration in the absence of respiration. The difference between noon and the extrapolated value gives the afternoon oxygen production (Figure 5.2, dark green bars). By adding the morning and afternoon quantities together and dividing by 1 d, the daily GOP in units of mmol m^{-3} d^{-1} is obtained. The respiration rate is known from the slope of the nighttime fits, and so the difference between GOP and R yields the NCP.

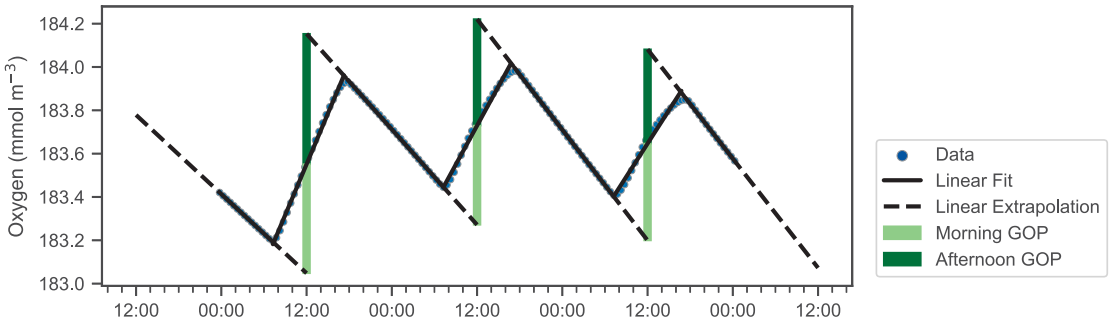

Figure 5.2: Schematic showing method for calculating GOP and R using oxygen data (points). Respiration rates are determined by the nighttime slopes (solid black lines), which are projected forward and backward (dashed black lines) in time to noon the subsequent and previous days. The difference between these projections and the observed noontime oxygen gives the morning and afternoon GOP (light and dark green bars respectively).

Typically, GOP and R have similar magnitudes and thus NCP will be small, often an order of magnitude smaller than the other two (*Westberry et al.*, 2012; *Ducklow and Doney*, 2013; *Nicholson et al.*, 2015). The initial application of this method was in the North Atlantic during the spring bloom where productivity was very high (satellite derived average NPP of 78 mmol C m^{-2} d^{-1} from 2012- 2015, *Behrenfeld and Falkowski*, 1997)

relative to the Gulf of Mexico (average NPP of 28 mmol C m^{-2} d^{-1} over the same period, *Behrenfeld and Falkowski*, 1997). Applying the method to the less productive Gulf of Mexico introduces new challenges.

A timeseries of mean euphotic zone oxygen from a continuous mode sampling period is shown as example in Figure 5.3. While oxygen is often changing periodically with increases during the day and decreases during the night, there also are several instances when oxygen changes cannot be reconciled with the expected day-night pattern of a biologically driven cycle. Light and dark red bars represent unrealistic negative gross production values (GOP, by definition, must be positive). This timeseries illustrates that in the study region, measuring diurnal cycles is not a simple procedure as other processes than biological production and consumption are affecting oxygen, confounding the production signal. Similar results were observed during other time periods and by other floats. Alternative physical drivers are explored further in Section 5.2.

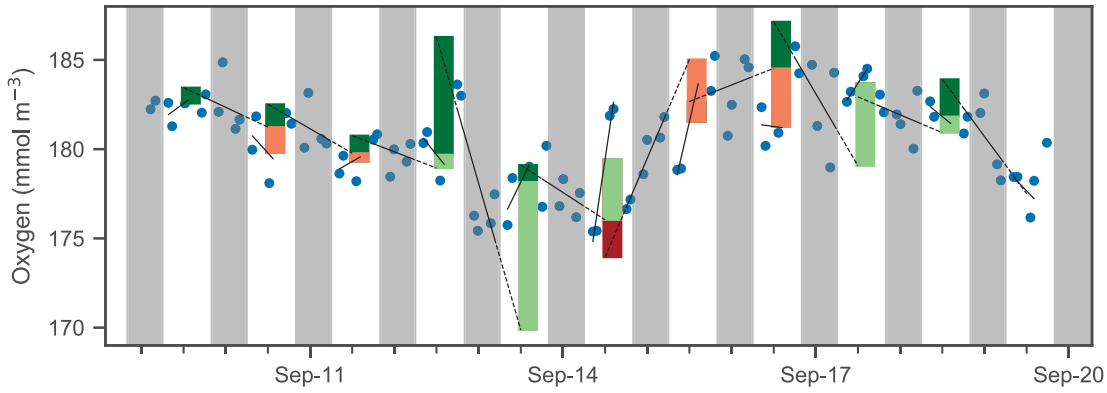

Figure 5.3: Mean oxygen values for the upper water column for continuous mode measurements in September made by float f8081, with attempts to estimate GOP. Light and dark red bars indicate where negative GOP is calculated, or when the method fails because other processes are driving changes in oxygen. Lighter colors are for morning production and darker for afternoon. Grey shaded sections show local nighttime. Similar results were shown by other floats and during other continuous mode sampling periods.

5.1.2 Model Analysis of Diurnal Oxygen Cycle

Next, the numerical model is used to show how this method would work in an ideal case and for different sampling frequencies and sampling errors. In ME2, the model is run using a basic setup to simulate the diurnal cycle of oxygen without vertical oscillations. The model simulation was run from May 2 to May 6, 2017, to match a continuous mode

analysis period for float f7940. The model was run through a spin-up period of one month leading up to the start date to reach steady state. At the start date, nitrate is re-initialized based on float observations of temperature and salinity, as is model temperature, salinity, and chlorophyll. The model state is saved every 30 min. From this model output, GOP, R, and NCP are derived following the method described in the previous section. Then the model is systematically subsampled at lower frequencies and with the addition of random observation errors to more accurately simulate realistic measurements.

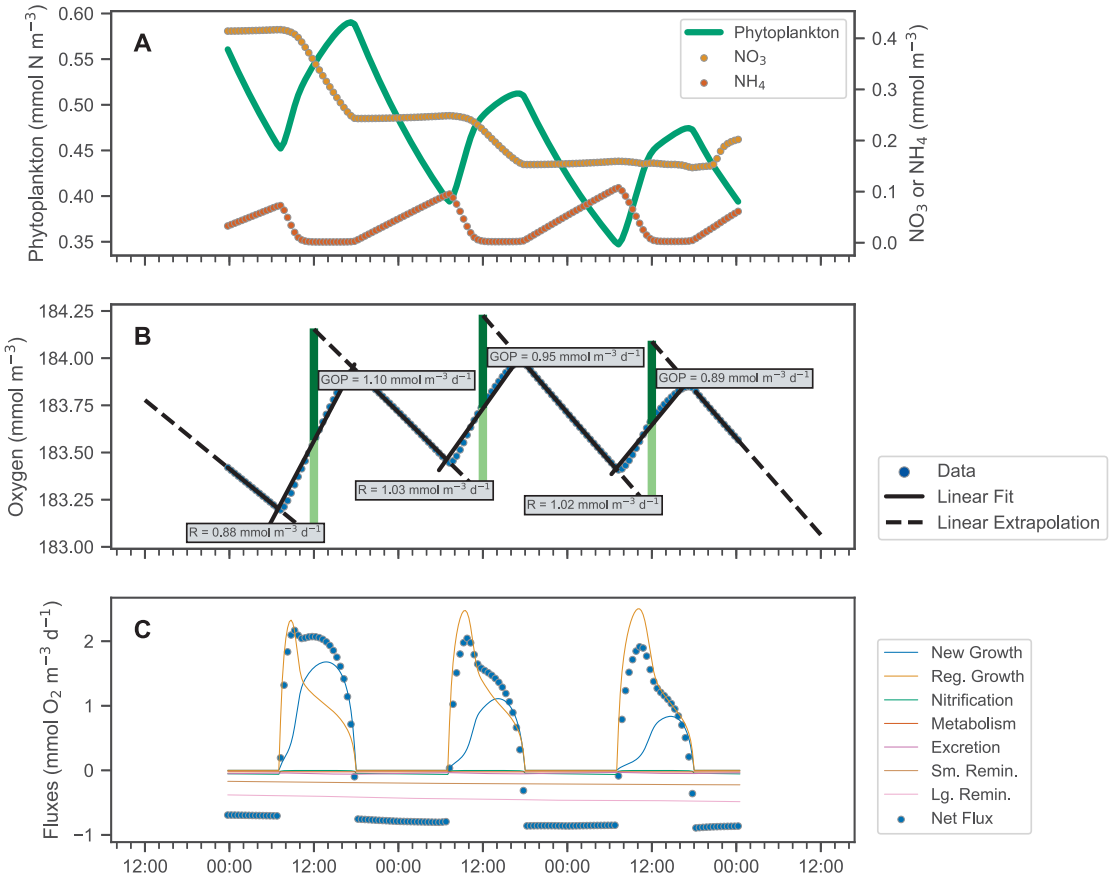

Figure 5.4: Simulated diurnal biological and oxygen cycle. (A) Simulated phytoplankton and nutrient concentrations in the mixed layer and (B) simulated mean oxygen in the top 150 m showing clear diurnal cycles. Also shown are nighttime linear fits extended to noon the previous and following days and daytime linear fits to oxygen for estimation of respiration and GOP. Respiration (R, lower labels) estimates are derived from the nighttime slope, and gross oxygen production (GOP, upper labels) estimates from the difference between extrapolated nighttime slopes and true noontime oxygen. (C) Contribution of individual processes to net oxygen flux in the model.

In the simulation, phytoplankton show a clear diurnal cycle in the mixed layer during the

continuous mode observation period (Figure 5.4A), which is mirrored by corresponding diurnal cycles in nutrient concentrations where NH_4 is depleted during the day and remineralized at night while NO_3 is drawn down during the day but remains steady at night. The NO_3-based growth rate decreases as NO_3 is drawn down. The simulated respiration is dominated by remineralization of small and large detritus. Regenerated growth (i.e. growth where NH_4 is the primary nutrient source) dominates photosynthesis.

Oxygen (Figure 5.4B) shows a clear day-night oxygen cycle, and GOP, R, and NCP can be extracted from the diurnal signal. GOP averages 0.983 mmol O_2 m^{-3} d^{-1}. Respiration averages 0.978 mmol O_2 m^{-3} d^{-1}. This results in a very small positive NCP value of 0.005 mmol O_2 m^{-3} d^{-1}.

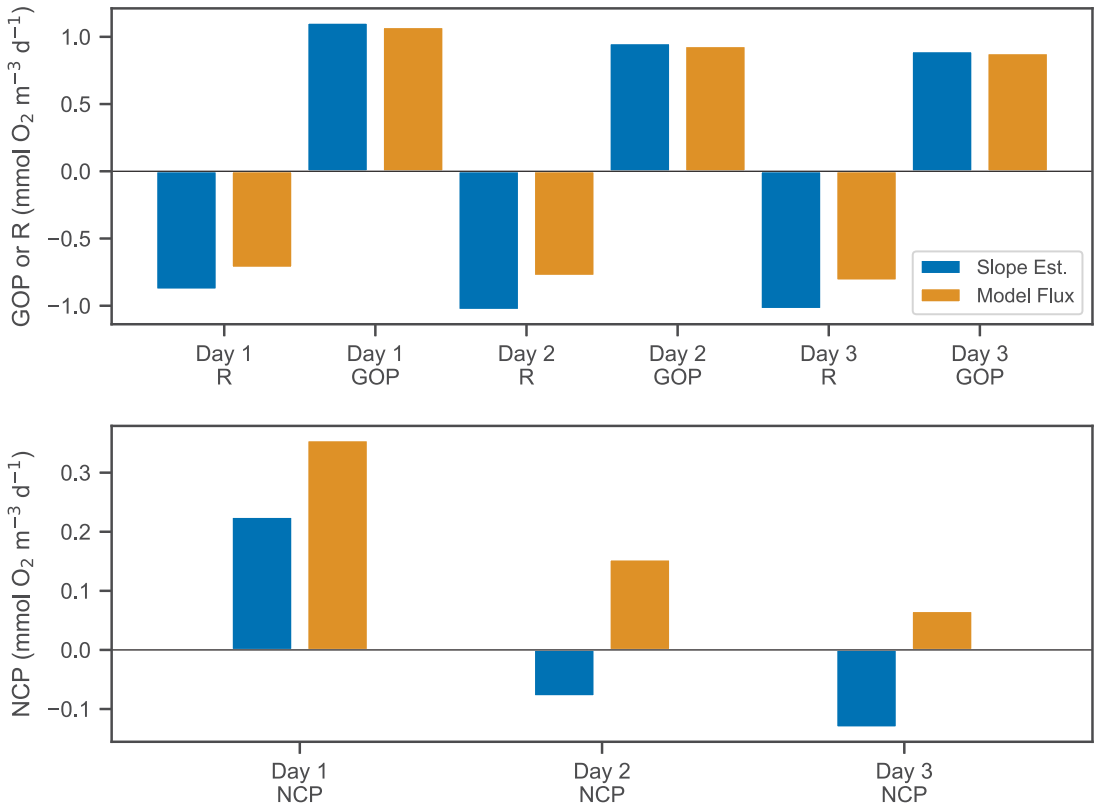

Figure 5.5: Comparison of slope-estimated and model flux production and respiration calculations. (A) GOP and R derived through the method described in *Briggs et al.* (2018) ("Slope Est."), and by directly analyzing the model flux output ("Model Flux"). (B) NCP derived through each method.

The values of GOP, R and NCP derived from the diurnal oxygen cycle can be compared directly to the simulated production and respiration fluxes, which are explicitly defined. In

figure 5.5, GOP, R, and NCP from the oxygen timeseries data ("Slope Est.", blue bars) are compared with those directly simulated by the model fluxes ("Model Flux", orange bars). The two methods show relatively good agreement for both GOP and R, however the slope estimation tends to be higher in magnitude for both fluxes. This small mismatch is likely due to two simplifying assumptions: (1) that oxygen will change linearly during the day and night (i.e. that GOP and R are constant), and (2) that air-sea flux can be neglected. The slope estimation technique tends to overestimate R by 25% and GOP by 1-3%. For both calculation methods, GOP and R are closely balanced and therefore NCP is small. For day 2 and 3 of the model simulation, the estimated NCP has the opposite sign from the true simulated flux. This demonstrates quite clearly the challenge in measuring a quantity like NCP that is a small difference between two significantly larger quantities. Given reasonable error on the contituent quantities, it will very difficult to accurately report a value for NCP.

Table 5.1: Total GOP, R, and NCP for different lower integration limits, and the percent of the total GOP on that interval.

z_{max}	GOP (mmol m^{-2} d^{-1})	R (mmol m^{-2} d^{-1})	NCP (mmol m^{-2} d^{-1})	% Total GOP
25	41.45	26.82	14.63	29.3
50	94.73	63.62	31.11	66.9
75	132.21	110.46	21.75	93.4
150	141.61	131.91	9.70	100

The model also allows an assessment of how estimates of GOP, R, and NCP would change if only the mixed layer is considered. In Table 5.1 and Figure 5.6, the effects of integrating to different depths are shown. Figure 5.6 shows that gross production is significantly higher than respiration in the mixed layer, and that both quantities are approximately constant in that layer (Figure 5.6A-B). As a result the total accumulated production and respiration increase linearly in the mixed layer as one integrates to greater depths (Figure 5.6C), and because R is less than GOP, the derived accumulated NCP increases (Figure 5.6D). When including values below the mixed layer, total GOP and R are tightly tied, with significantly reduced GOP and still relatively consistent R down to 100 m. When integrating to the average mixed layer depth (about 50 m), only 2/3 of the total GOP is captured, and only about 1/2 of the total respiration. This leads to an overestimation of NCP compared to the vertically integrated value. The correct estimate

of NCP is in fact about 3 times smaller than it would be if only the mixed layer were considered. When integrating to a depth of 100 m, the values for GOP, NCP and R converge in the model (Figure 5.6).

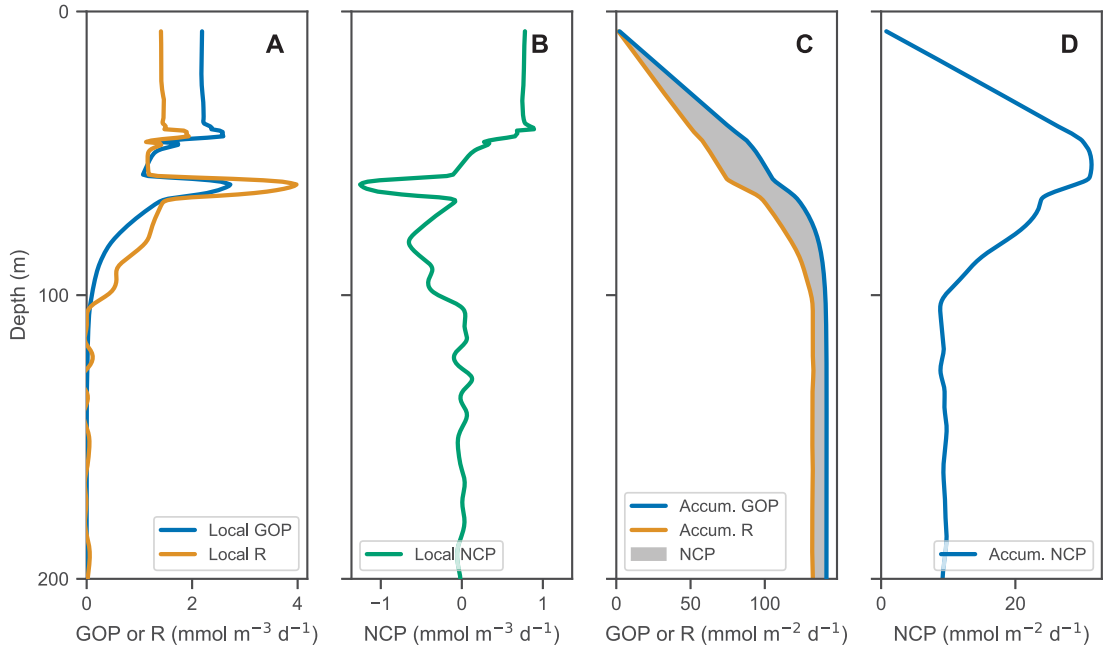

Figure 5.6: GOP, R, and NCP profiles and integration analysis. (A) Profiles of local GOP, R. (B) Profile of local NCP. (C) Cumulative GOP and R for increasing integration depths, with the resulting NCP shown in the shaded region. (D) Cumulative NCP for increasing integration depths.

Next, I address the question of how many profiles are needed over a 24-hour day/night cycle to reliably estimate GOP, R, and NCP given measurements errors and other potentially contaminating signals. Measurement errors are investigated in the following section, and the imprint of physical processes is analyzed and discussed in more detail in Section 5.2.

5.1.3 Sampling Frequency and Error Analysis

An important question is how well the diurnal cycle can be observed for different sampling frequencies and measurement errors. To address this question, random error of various magnitudes is introduced to the output of ME2 and the model sub-sampled at different frequencies. Errors are randomly generated on a normal distribution surrounding zero for increasing standard deviations (error magnitudes):

$$\epsilon \sim N(0, \sigma), \quad \sigma \in (0.01, 0.3) \tag{5.2}$$

These model experiments seek to characterize what combination of sampling frequency and signal-to-noise ratio allows the GOP, R, and NCP to be reliably estimated.

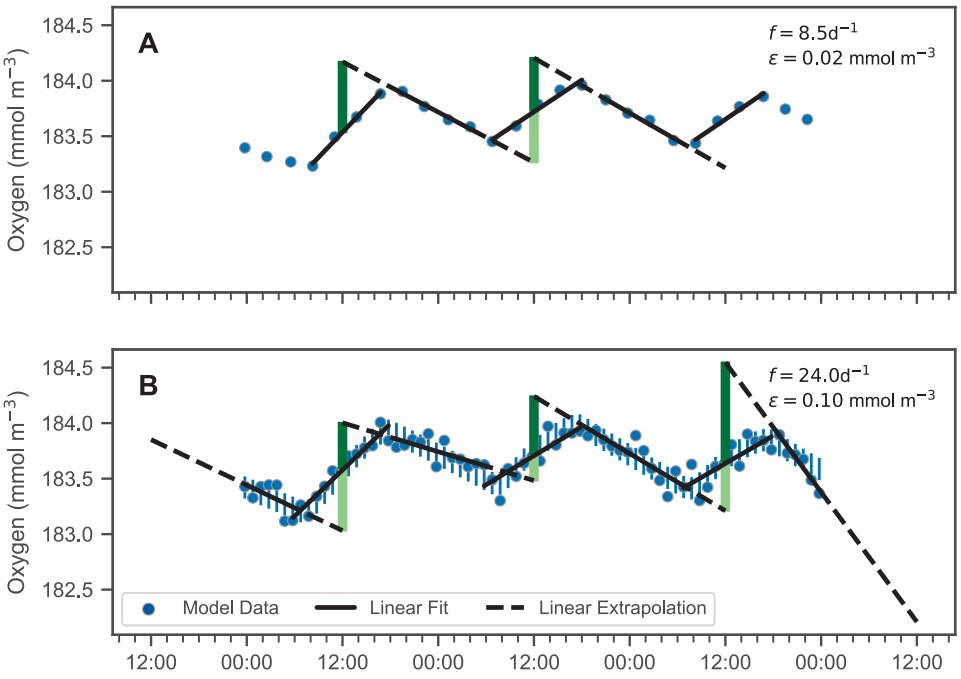

Figure 5.7: Example mean oxygen timeseries for two different sampling frequencies and errors. Error bars show the assumed standard deviation of the random measurement error centred on the true value. Blue dots show the simulated measurements.

Model output is sampled at frequencies f_i varying from once per hour (24 d^{-1}) to once every 3 hours (8 d^{-1}). At frequencies lower than 8 d^{-1}, linear fits would have to be applied to fewer than 4 data points which does not seem reasonable. Standard deviations for random errors range in magnitude from 0.01 mmol m^{-3} to 0.3 mmol m^{-3}. As metric to evaluate each combination of error and sampling frequency the absolute percent deviation (eq. 5.3) from the ideal case (high sampling frequency of 96 d^{-1} and no error) is used:

$$\%GOP(f_i, e_i) = 100 \times \left| \frac{GOP(f_i, e_j) - GOP(96, 0)}{GOP(96, 0)} \right| \tag{5.3}$$

The calculation for each combination of frequency and noise is replicated 50 times.

The greatest deviations are seen, unsurprisingly, for large errors and low sampling frequencies. Higher sampling frequency mitigates the effects of measurement error to some degree. This is most easily seen by examining the 50% contour line in Figure 5.8B, as slightly lower error magnitudes result in 50% absolute deviation when sampling 8 times per day compared to 24 times per day.

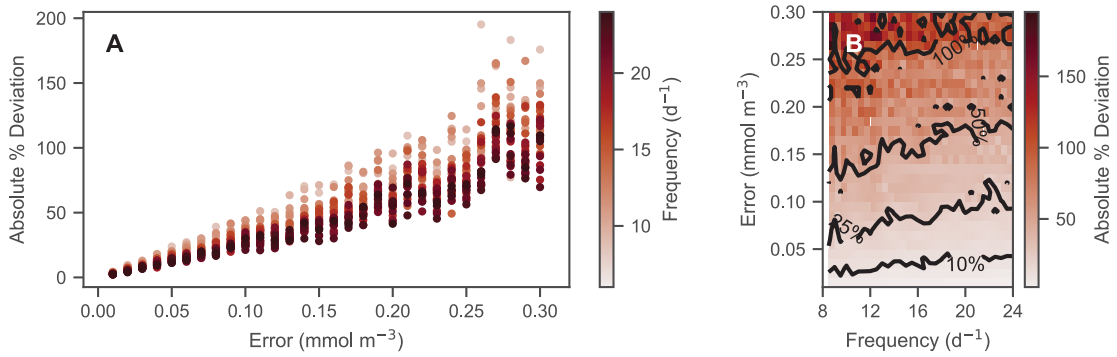

Figure 5.8: Mean absolute deviation in percent for different sampling frequencies and random errors.

5.1.4 Discussion

The data and analysis presented in this section have shown that diurnal changes in oxygen can be measured with a profiling float; however, the changes observed here could not unequivocally be linked to biological production and respiration. This made estimates of daily GOP, R, and NCP based on these observations unreliable or impossible. Compared to previous work by *Briggs et al.* (2018), which focused on diurnal oxygen cycles in the North Atlantic spring bloom, the Gulf of Mexico has relatively low production (by about one third). *Nicholson et al.* (2015) studied diurnal oxygen cycles in a similarly low-productivity region in the subtropical North Pacific, but accumulated and averaged many days in order to derive an estimate of production.

The timing and location of the continuous mode observations also may have caused difficulty in estimating production. Continuous mode was turned on for the floats when storms were passing through the Gulf. Higher wind forcing likely caused physical drivers (explored further in Section 5.2 to dominate the oxygen signal. Additionally, the floats were deployed close to the Deepwater Horizon oil spill site, near the shelf break of the Gulf. Topography is a significant factor contributing to the formation of internal motions

(*Alford et al.*, 2016), and the topography near the float locations may have encouraged dominance of physical drivers.

Despite continuous profiling by the floats, the temporal resolution was on the low end for making diurnal measurements. In continuous mode, the floats still recorded full profiles to at least 1000 m because of other research objectives. In a study more directly focussed on diurnal oxygen cycles, profiling to only 200 m would significantly increase the temporal resolution of the oxygen timeseries, while still capturing the entire euphotic zone.

Model analysis shows that using diurnal oxygen timeseries to estimate GOP, R, and NCP is not perfect, likely due to the assumption that production and respiration are constant rates, when in reality they change over the course of a day, and because air-sea flux of oxygen is neglected. NCP is especially difficult to estimate in a system where gross production and respiration are closely balanced. NCP is often an order of magnitude smaller than GOP and R, and so any error in those two larger quantities will lead to large relative error in the difference between the two. This is demonstrated when calculating the NCP in the model, where the calculation method yielded the wrong sign of NCP on some days (figure 5.5). In cases where NCP is large, such as during phytoplankton blooms, the relative error in NCP should be smaller. In systems where GOP and R are closely balanced, other approaches such as measuring oxygen changes below the mixed layer (*Riser and Johnson*, 2008), calculating mass-balances in the upper ocean (*Plant et al.*, 2016), or averaging over many days (*Nicholson et al.*, 2015) may be preferable.

Model results also showed that estimating integrated NCP using only mixed layer measurements lead to significant overestimates of net production. Depending on the integration limit, NCP was overestimated by up to a factor of 2.5. Clearly, this demonstrates that consideration of processes at greater depths than the mixed layer is important when trying to estimate the total water column NCP. For measurements confined to the surface such as with mixed layer floats, $[O_2]$/[Ar] measurements, or beam-c measured by ship underway flow-through, estimations of production must be discussed in the context of the mixed layer only. Extending or integrating these quantities may prove to be unreliable.

Analysis of sampling frequency and random measurement error suggests that at least 8 profiles per day are required; however, increases in sampling frequency do not strongly mitigate the negative effects of random error. Results show that when measuring 16 profiles per day, a 50% absolute deviation between true and estimated GOP occurs at a

random error with 0.15 mmol O_2 m^{-3} standard deviation. This small error represents 15% of the magnitude of the diurnal oxygen cycle of 1 mmol O_2 m^{-3}. In a more productive system, like the North Atlantic where Briggs et al. (2018) observed GOP up to almost 18 mmol O_2 d^{-1}, the 50%-error threshold would be much larger at about 2.5 mmol O_2 m^{-3}.

Analysis of profiles recorded by the autonomous floats has clearly shown that estimating productivity from diurnal changes in oxygen can be difficult because of the influence of other confounding processes.

5.2 Physical Drivers of Dissolved Oxygen Variation

In the following subsections, three major physical drivers that influence oxygen are described. Each driver expresses itself in the float data in a different way and presents a major influence on dissolved oxygen dynamics. These drivers are discussed in the context of the overarching goal of observing biological changes in oxygen.

5.2.1 Vertical Oscillations

Vertical oscillations of isopycnals may occur in ocean environments due to several processes including internal or near-inertial waves, barotropic or baroclinic tides, and mesoscale eddies. These processes are ubiquitous in the ocean and can have a significant effect on the vertical structure of biogeochemical properties. For oxygen, isopycnal displacement pushing the gradient up and down will create a periodic signal in integrated oxygen over time, at the same frequency as the oscillations. The oscillatory period will be near 24 h due the Coriolis frequency at this latitude (*Alford et al.*, 2016), and so caution must be exercised as to not misconstrue the physical oscillatory signal with a biological one.

Vertical oscillations were present in the float data in many cases. As an example, a 3-day period immediately following the deployment of float f7940 on May 2, 2017 is examined here. This float was deployed shortly before passage of an atmospheric front with elevated wind speeds up to about 35 km h^{-1}. The float remained in deep (greater than 1000 m) waters off-shelf for the period discussed here. Vertical oscillations are apparent by coincident up and down movements of the oxygen gradient moving in concert with isopycnals. A tight correlation of oxygen and isopycnal (or isotherm) depths can be used to identify when a physical process inducing vertical motion is driving changes in oxygen.

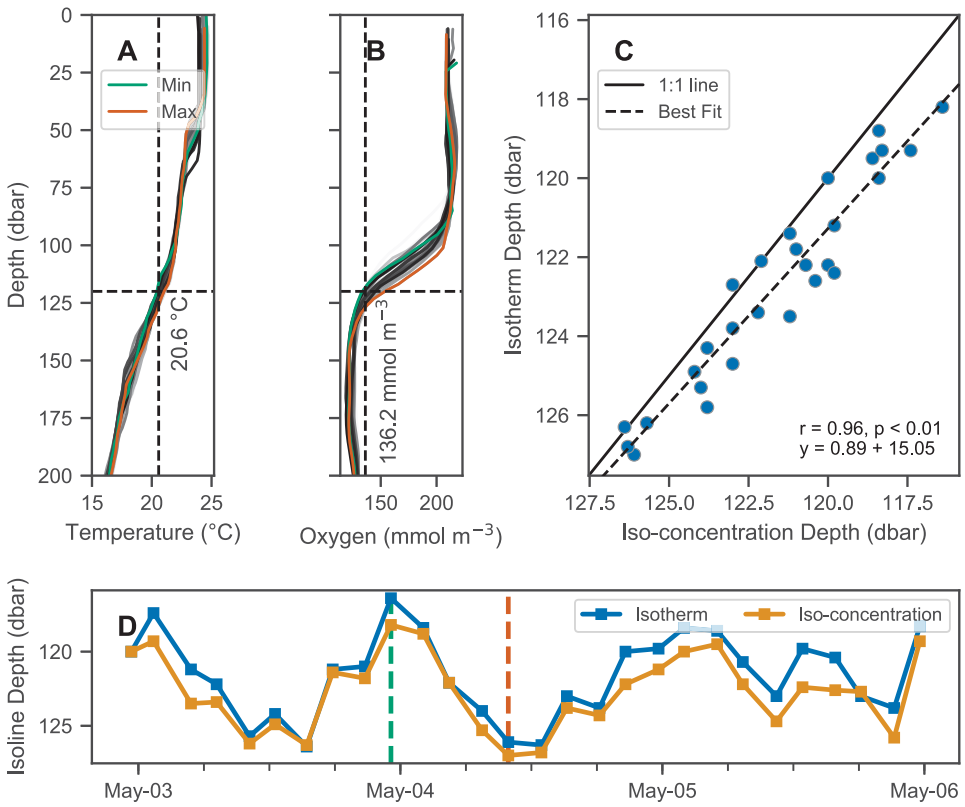

Figure 5.9: Co- variation of isotherm and iso-concentration depths. (A-B) Profiles of temperature and dissolved oxygen, where the profiles with the minimum and maximum depths of the 20.6 °C isotherm and 136.2 mmol m^{-3} iso-concentration are shown in green and orange respectively, and all other profiles are shown on a grey color scale indicative of time with lighter shades indicating older and darker shades more recent measurements. (C-D) Depths of the isotherm and iso-concentration plotted against each other in (C) and as a timeseries in (D), showing their co-variation.

The tight correlation from vertical oscillation is shown in Figure 5.9. The profiles show that the changes in integrated oxygen are being driven by oscillatory changes in depth of the oxygen gradient. These changes are reflected in the physical variables as well, as temperature and salinity profiles display similar periodic oscillations up and down. The depths of the 20.6 °C isotherm and 136.2 mmol m^{-3} iso-concentration are highly correlated over this time period (Figure 5.9C, $r = 0.96$, $p < 0.01$). The timeseries of these depths are also highly correlated with the timeseries of integrated oxygen (Figure 5.10, $r = 0.83$, $p < 0.01$). The extrema are aligned as well, as the maximum depths of the isotherm correspond with the maximum values of integrated oxygen, and similarly minimal depths correspond to integrated oxygen minima, occurring near noon and at midnight, respectively.

Since the vertical movement of isopycnals and oxygen isolines creates a tight correlation between the two, it should be possible to remove the variability due to vertical motions by analyzing changes in oxygen in density space rather than pressure space. Figure 5.11 shows the anomalies calculated in pressure and density space compared to each other, and density anomalies are significantly smaller, indicating that most of the variability in oxygen can be accounted for by corresponding changes in density. This technique offers a path to removing the oscillatory signal, and therefore isolating underlying signals such as biological production. In this case, however, the remaining anomaly is on the order of expected errors based on the analysis performed in Section 4.3, and so a biological signal cannot be discerned in light of the accumulated error.

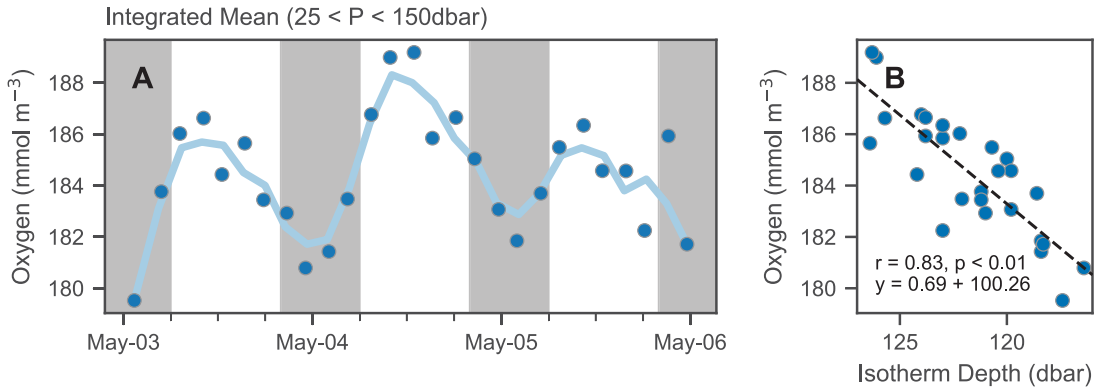

Figure 5.10: Isotherm depth and mean oxygen comparison. (A) Timeseries of mean oxygen between 25-150 dbar. A period of about 24 h is observed, however it is not in phase with the day/night cycle (nighttime indicated by shaded areas) as would be expected for a biological signal. (B) Scatter of mean oxygen concentration against isotherm depth (see figure 5.9D).

Not only can isopycnal displacement confound the biological signal, it may also alter the behaviour of production in the water column. Using the numerical model, ME3 explores the interaction of the biologically driven diurnal oxygen cycle and vertical oscillations. The model is run with the vertical oscillations set to be “in-phase” with the diurnal oxygen cycle (isopycnals nearest to the surface at noon, deepest at midnight), and “out-of-phase” with the cycle (isopycnals nearest to the surface at midnight, deepest at noon). For each run, the influence of the vertical oscillations on the biological cycle is evaluated.

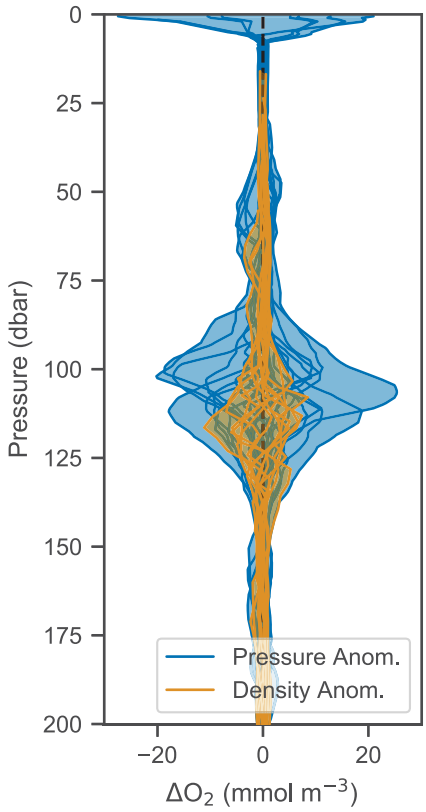

Figure 5.11: Anomalies calculated in pressure (blue) and density (orange) space.

The results in figure 5.12 show a mean oxygen signal dominated by vertical oscillations, and relatively small differences in biological fluxes between the two runs. The greatest differences appear at the extrema when the isopycnals are at opposite extremes, and almost no difference when they cross each other.

5.2.2 Horizonal Advection

Circulation within the Gulf may result in dramatic changes in oxygen water column structure given differences in physical or biochemical signature. This is especially true in the eastern part of the Gulf where the Loop Current intrudes and may shed eddies, and near the northern shelf where river runoff makes the environment more eutrophic than the open Gulf. In the profiling float data, the collision of different water masses should be evident in both the physical and biochemical properties. Changes in the temperature-salinity signature should be indicative of water masses of different origin noting that water in the open Gulf of Mexico, especially at depth, has a very tight T-S relationship that can be identified. Deviations away from this should be a good indicator of shelf water.

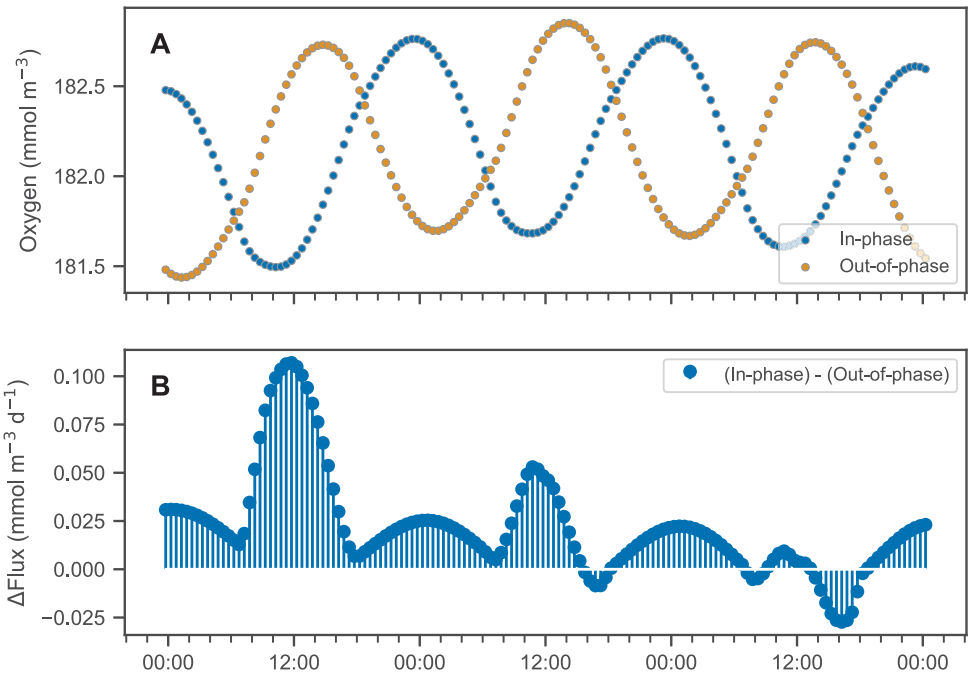

Figure 5.12: Model comparison for vertical oscillations in- and out-of-phase with biology. (A) Mean oxygen for "In-phase" and "Out-of- phase" vertical oscillations. (B) Difference between fluxes for in-phase and out-of-phase.

An example of water masses with unique physical and biochemical signatures colliding is provided by float f7942 during October 6-9, 2017. This particular float had drifted northeast close to the shelf since the time of its deployment and was travelling along the 200 m isobath. The profiles recorded by the float show significant changes in vertical structure, specifically deformation at a depth of 100 m (Figure 5.13A- 5.13C). As this deformation occurs, oxygen increases during two distinct periods: the afternoon/evening of October 6 and climbing consistently after noontime on October 7 through to the afternoon of October 8 (Figure 5.13D).

The initial oxygen profile shows a relatively shallow and steep oxycline near 50-75 dbar, around the bottom of the mixed layer. The gradient becomes much broader over time, spreading down to about 150 dbar. This change occurs below the MLD , which remains at about 50 dbar throughout. The broadening of the oxygen gradient is likely influenced by elevated winds during this time period as 6 h average winds reached up to 50 km h^{-1}. The deformation is not simply a redistribution of oxygen by vertical mixing, as the mean oxygen is rising during the same period.

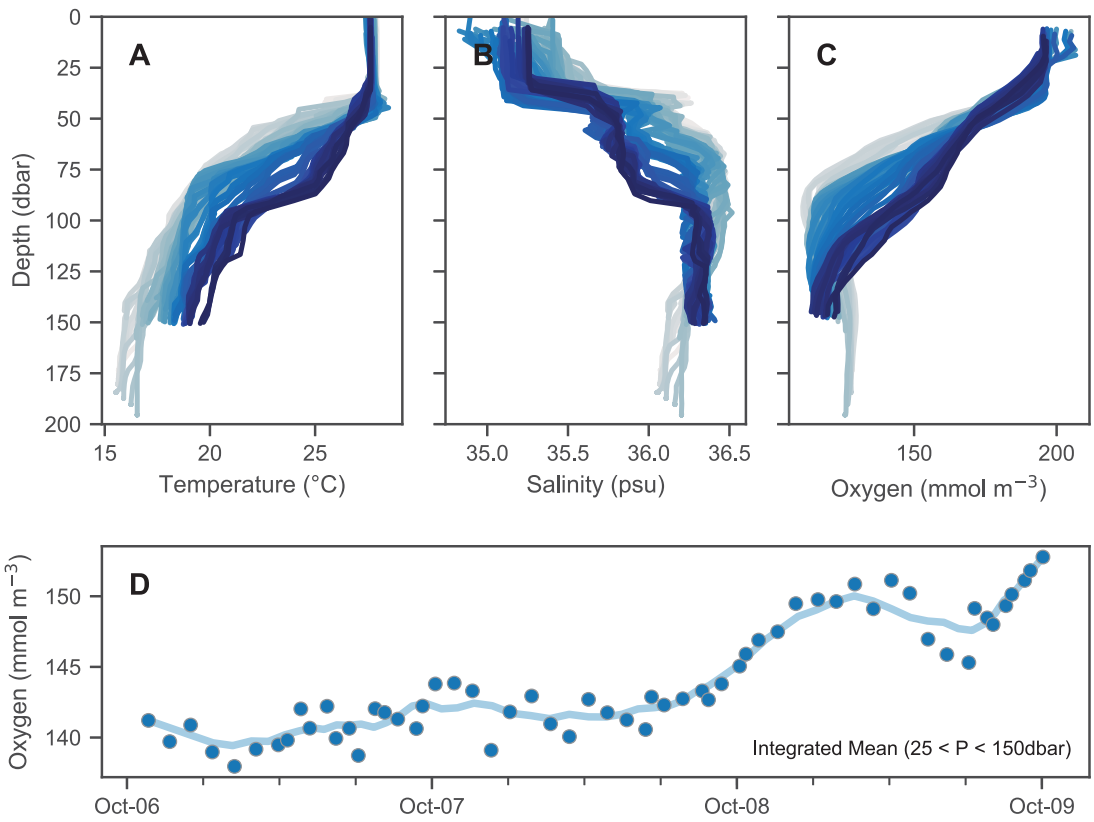

Figure 5.13: (A) Temperature, (B) Salinity, (C), and Oxygen profiles during October 6-9, where deeper blues represent later dates, showing the progression of the profiles. (D) Mean oxygen from 25-150 dbar.

Figure 5.14 shows a T-S diagram for all the profile data, where points are coloured for their oxygen anomaly and elapsed time in the analysis period. Oxygen anomalies are calculated using interpolated profiles every 5 dbar. Over time, the middle of the water column shifts to fresher, warmer water with a higher oxygen content. The surface remains relatively consistent, with some variations in salinity but steady temperature and oxygen values, and the MLD does not change.

Two water masses with unique physical and biochemical footprints caused deformation of profiles, and a significant increase in mean oxygen of 10 mmol m^{-3} over the top 150 dbar of the water column. Based on the synchronous shift of temperature, salinity, and oxygen below the mixed layer, this change could not be the result of a biological process. With the increase in mean oxygen, this could also not simply be a vertical mixing of the water column.

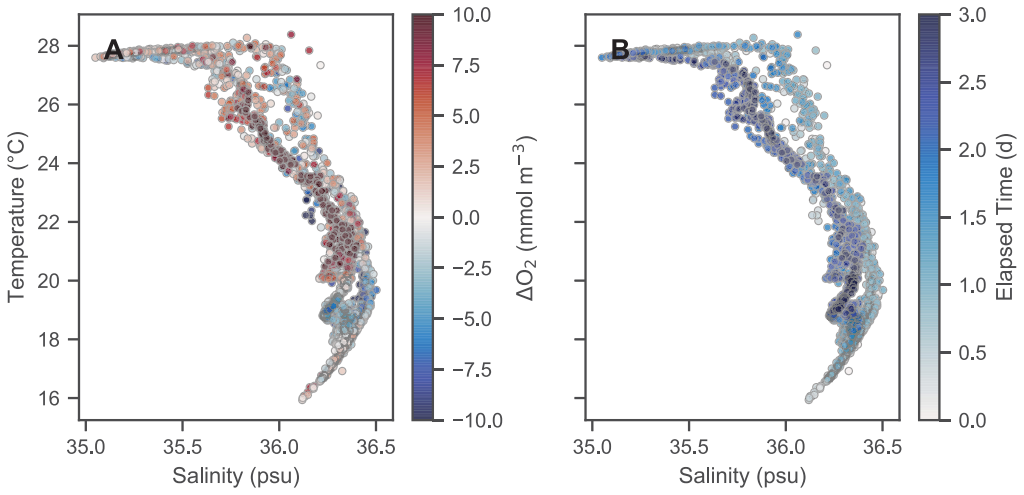

Figure 5.14: T-S diagram for profile data recorded during this observation period (Oct. 6-9, 2017), where the colorscale represents the (A) oxygen anomaly or (B) elapsed time in analysis period.

5.2.3 Deepening Mixed Layer Depth

Mixed layer dynamics can strongly influence biological production, as a deepening of the mixed layer can induce an injection of nutrients from below, triggering potentially massive growth in the euphotic zone. In the open Gulf of Mexico, this mechanism is less prevalent as waters are nutrient- poor. Changes in the mixed layer depth may still influence oxygen dynamics, but through physical rather than biological changes.

A deepening mixed layer was observed by float f7943 over an 8-day period during the passage of Hurricane Nate, from October 4-12, 2017. During this period, the float was relatively stationary, and like some other floats, had drifted toward the shelf between the 200 and 500 m isobaths. Mean oxygen increased steadily and then leveled off around October 8. Mixed layer depth followed a similar trend deepening steadily from about 20 m to 70 m until October 8, then oscillating around about 65 m (Figure 5.15A). Mean oxygen and mixed layer depth are highly correlated ($r = 0.88$, $p < 0.01$, Figure 5.15B), with the deepest of MLDs corresponding to the highest mean oxygen concentrations and vice-versa.

In addition to the mean increase in oxygen, there is an underlying periodic signal. This oscillatory signal has a period of 18.5 h per spectral analysis. A similar analysis of isotherm and iso-concentration depths to that in Section 5.2.1 (Figure 5.9) showed very high correlation between the two, including both the deepening of both isolines and the

oscillations on the shorter timescale (Figure 5.16).

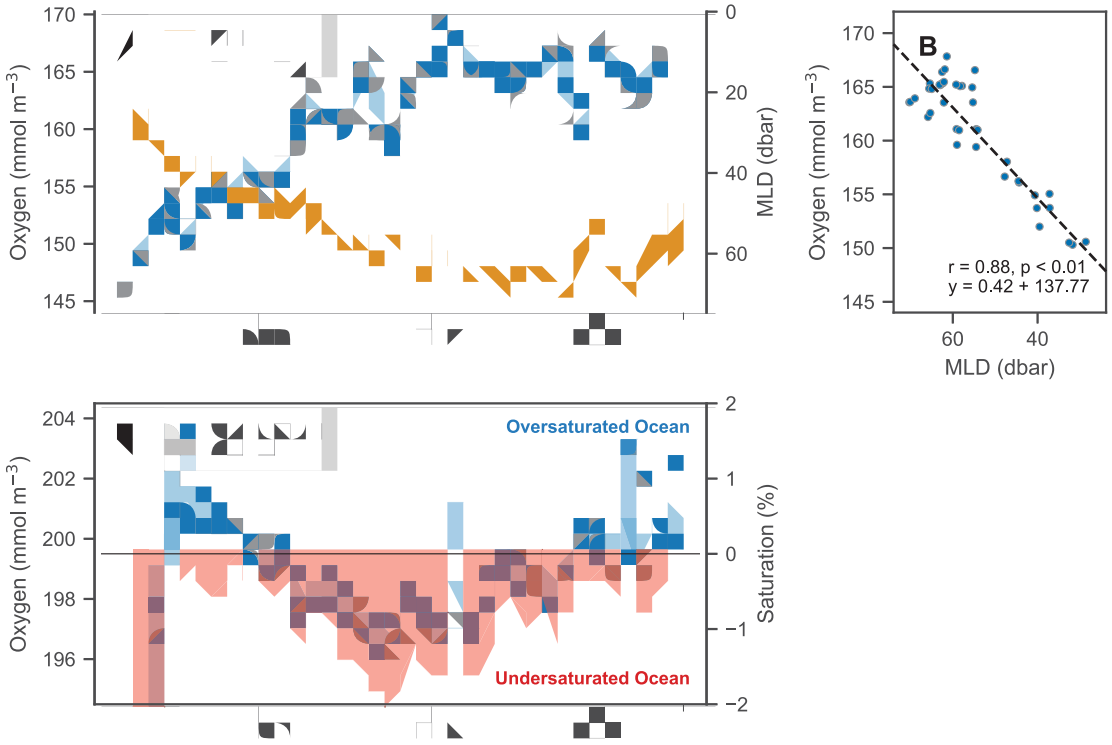

Figure 5.15: Mean oxygen, mixed layer, and surface oxygen concentration and saturation. (A) Mean oxygen (left axis) and mixed layer depth (right axis). (B) Scatter of MLD and mean oxygen shows maximum oxygen values for deepest mixed layers. (C) Surface oxygen (left axis) and surface layer saturation percent (shaded area, right axis) where the horizontal black line shows ocean and atmosphere in equilibrium, positive values indicate an oversaturated ocean, and negative values an undersaturated ocean.

Biological and atmospheric sources of oxygen were considered to explain this large mean increase of more than 20 mmol m^{-3} in oxygen, but neither was found to support such a significant change. Biologically, mean oxygen and chlorophyll in the mixed layer showed no correlation, while oxygen and baseline backscatter were inversely correlated. While pigment concentration does not necessarily have to change with biomass, depending on the conditions (*Cullen*, 2015), baseline backscatter representing suspended biomass would be expected to increase if algal growth was indeed the source of net oxygen changes in this case.

Air-sea gas exchange is driven by the gradient in partial pressure of oxygen between the surface ocean relative to the partial pressure of the atmosphere, and proportional to wind stress. Calculations of air-sea gas exchange are included in the model following the

parameterization of *Wanninkhof* (1992). The surface layer is under- saturated throughout the observation period (Figure 5.15C) and air-to-sea flux of oxygen does occur, however it is small relative to the total increase in mean oxygen. Surface oxygen is *decreasing* up to October 8 (Figure 5.15C), where maximum air-sea flux occurs. In contrast, the mean oxygen is *increasing* up to October 8, and most levels off afterwards (Figure 5.15A). Air-sea flux may contribute to maintaining the plateau of mean oxygen concentration but is not the primary driver of change in this case.

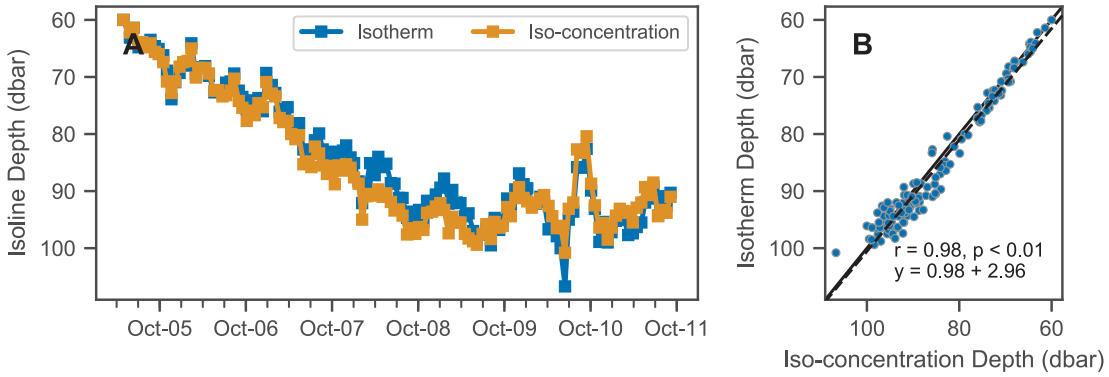

Figure 5.16: Timeseries (A) and scatter (B) of the 21.6 °C isotherm and 144.7 mmol m^{-3} iso- concentration depths during the deepening mixed layer. Scatter of the two depths show highly correlated changes in each isoline depth ($r = 0.98$, $p < 0.01$).

Physically driven changes in oxygen via the mixed layer should not prevent the measurement of the diurnal biologically driven changes occurring at the same time. The change in the mixed layer will induce a change in the mean oxygen at a rate proportional to the rate of change of the mixed layer. If this timescale is sufficiently long, the physically driven change will not interfere with the detection of a biological diurnal scale change. The diurnal scale change was not able to be resolved in the data presented here not because of the mixed layer change, but due to the underlying vertical oscillation signal.

5.2.4 Discussion

Vertical oscillations, horizontal advection, and a varying MLD all influence euphotic-zone oxygen in different ways and have different implications for the measurement of biologically driven changes. In attempting to measure biological productivity using oxygen, it is important to understand, and take into consideration, the effects of physical drivers. In general, all available data recorded by the float should be visualized during analysis to

obtain the most complete view available of physical and biogeochemical changes in the water column. Here, I propose specific ways in which to visualize float data to recognize and accommodate for physical influences on the biochemical data.

Vertical oscillations can be identified in float data by observing the synchronous movement of physical and biochemical variables in the water column. When it is identified, the characteristically tight correlation of density and oxygen may still allow for the isolation of the underlying biological signal. Although the vertical oscillation signal can mostly be captured by variations in density (Figure 5.11), the remaining signal cannot always be attributed to biological changes in the water column. For our data, this analysis showed anomalies on the same scale as expected error from the oxygen optode. The error sources associated with oxygen measurements on autonomous floats discussed in Section 5.1.4 can create deviations on the scale seen in observations, meaning that those observed anomalies may not be representative of real oceanographic processes, but rather are an artefact of the measurement process. In *Plant et al.* (2016), evidence of internal waves was also present in the data, and a similar method was used to remove this signal. In their case, using density to map the observations to a physical model that did not include vertical oscillations, it was possible to isolate the biological signal.

Near 30° latitude where the autonomous floats in this study were deployed, an external physical force acting on a resonant system will generate oscillations with a period of about 24 h. In this case, the most likely driver is elevated winds acting on this region with variable topography (*Alford et al.*, 2016), however other sources could create a very similar response. Without consideration of the physical data, and only of the oxygen oscillations, if this oscillation was aligned with the expected day-night cycle could falsely appear to be driven by biological productivity.

The diurnal-scale period of the internal oscillations could be problematic if production had been estimated by accumulating and averaging data on a one-day scale, as in *Nicholson et al.* (2015). This study quantifies average NCP over a 110 day period by accumulating glider measurements of oxygen and plotting them all on the same 24 h timescale. Only oxygen data that fit the theoretical biological curve defined *a priori* to a satisfactory degree ($p < 0.05$) are accumulated (73 of 110 days satisfied this condition). This is a good way to eliminate data where biology is not the primary driver, but could also eliminate days of smaller magnitude production, or allow physically driven oscillations that are aligned with

the day-night cycle to be attributed to biology.

In cases where there is evidence of horizontal advection dominating the water column dynamics, a reliable measurement of production cannot be performed. In calculating production from profile data, one of the key assumptions is that change is that horizontal influences are minimal. As soon as this assumption does not hold, any calculation using the method described here will be unreliable. Horizontal advection can be recognized in the profiling data by a deformation of profiles in time, and by a shift in temperature-salinity space with a corresponding shift in the biochemical tracer of interest, oxygen in this case. Horizontal advection is most important in cases like the one presented in Section 5.2.2 where water masses with unique physical and biochemical properties come together. Horizontal advection of homogenous water masses will not manifest itself in the measurements in the same way and may no be detectable.

Changes in MLD may change the mean oxygen in the upper water column (depths shallower than 150 dbar), however should not impede the calculation of GPP, R, and thus NCP. The changes observed here highlight how an integrated measurement of oxygen is important to obtain a full view of oxygen dynamics in the upper ocean. The data presented in Section 5.2.3 and Figure 5.15 show the increase of mean oxygen with the deepening mixed layer. If a local measurement only was presented, oxygen would appear relatively constant.

When working with biogeochemical observations, the coincident physical measurements should be taken into account to gain a full view of the ocean state and how it is changing. In some cases, it may be possible to correct for or remove the physical signal, while in others physical processes may be dominating oxygen changes in the water column to a degree that prohibits biological inferences.

CHAPTER 6

CONCLUSION

In the Introduction, the question "Can GPP, R, and NCP be estimated from the diurnal oxygen cycle measured by continuously autonomous profiling floats?" was posed. This research question contains two main components: (1) the technical question whether the sensor and platform can take sufficiently frequent and accurate measurements, and (2) the oceanographic question of what primary physical or biological processes drive changes in dissolved oxygen, and how they manifest themselves in the data. Addressing (1) led to the development of a novel method for determining the effective *in-situ* time constant of an oxygen optode deployed on a profiling float, without needing to characterize the physical flow around that sensor. Component (2) was addressed through a comprehensive analysis of the physical and biochemical measurements in a case study in the Gulf of Mexico that will lend context and techniques to future studies seeking to quantify production using profiling floats.

Oxygen optodes are challenged to make accurate measurements in gradients because of their slow response time. However, the resulting errors can be corrected if timestamps of the measurements and the effective response time are known. I developed an optimization procedure to determine the effective time constant in-situ by using both the up- and down-casts measured by the floats. The effective time constant determined in the field represents the combination of the inherent sensor response time, the response time that results from boundary layer effects in the flow field around the sensor, and any temperature, salinity, or pressure effects on response time. The time constants derived by this method are similar to estimates provided in previous literature for boundary layer response times on floats (Section 4.4). While the oxygen measurements were improved significantly by the

correction procedure, remaining errors, especially near gradients, may prohibit reliable production estimates in low productivity environments or where physical processes have large effects on the oxygen signal.

Given the small productivity of the Gulf of Mexico, oxygen optodes on autonomous floats were not able to provide sufficient precision to estimate production on a diurnal scale, resulting from a combination of sensor error and the surrounding dynamics driving non-biological change in oxygen. For processes like the vertical oscillation of isopycnals, analysis in density space can reveal underlying signals, and the anomaly technique employed in this research may be useful in calculating diurnal scale biological changes in oxygen in environments where the magnitude is much larger than the cumulative sensor error. In the absence of these confounding processes, measurements of GOP and R may be reliably made, however in steady-state systems where the magnitudes of each constituent quantity are comparable, NCP will likely still prove difficult to calculate.

The need for highly accurate, corrected oxygen measurements when estimating production from autonomous platforms leads to the following recommendations for future deployments of autonomous floats with oxygen optodes:

- Include timestamps for every oxygen measurement on float data transmission. The corrections discussed and applied here must be performed on oxygen as a timeseries, not as a profile. Correction for sensor response time is impossible without this information.

- Program the float mission to include a calibration period upon float deployment where both up- and down-casts are recorded. This will provide a very practical and robust method to calculate the effective in-situ response times.

This research shows that although taking an integrated measurement of oxygen below the mixed layer depth may include processes that introduce abiotic contributions on the diurnal scale, neglecting the full vertical structure can lead to poor estimates of NCP. Local measurements may resolve diurnal scale variations more readily, but an estimate of the entire water column production cannot be made. Production measurements can be difficult, laborious, and expensive to obtain, and making such measurements without including the entire water column results in an inaccurate measurement for such intensive work. As

sensor technology and our understanding of processes driving changes in oxygen improve, an integrated measurement should be the goal moving forward.

APPENDIX A

NUMERICAL MODEL EQUATIONS

The temporal evolution of phytoplankton due to biological sources or sinks is given by:

$$\begin{aligned}\frac{\partial Phy}{\partial t} &= \mu Phy - gZoo - m_P Phy - \tau(SDet + Phy)Phy \\ &\quad - \frac{\partial}{\partial z}\Big(k_z \frac{\partial Phy}{\partial z}\Big) - w_P \frac{\partial Phy}{\partial z}\end{aligned} \tag{A.1}$$

The growth rate μ depends on the maximum growth rate as defined by temperature (*Eppley*, 1972), the photosynthetically available radiation, I, and concentrations of nutrients NO_3 and NH_4:

$$\mu = \mu_{max} \cdot f(I) \cdot (L_{NO_3} + L_{NH_4}) \tag{A.2}$$

where:

$$L_{NO_3} = \frac{NO_3}{k_{NO_3} + NO_3} \cdot \frac{1}{1 + NH_4/k_{NH_4}} \tag{A.3a}$$

$$L_{NH_4} = \frac{NH_4}{k_{NH_4} + NH_4} \tag{A.3b}$$

Surface light levels I_0 are calculated using the astronomical formula. Below the sea surface, light decays exponentially with depth according to:

$$I = I(z) = I_0 \cdot r_{PAR} \cdot \exp\Big(- z\Big[K_w + K_{Chl} \int_z^0 Chl(\zeta) d\zeta\Big]\Big) \tag{A.4}$$

where r_{PAR} is the fraction of photosynthetically available radiation, 0.43, and K_w and K_{Chl} are the light attenuation coefficients of water and chlorophyll respectively. The function $f(I)$ in equation A.2 is the photosynthesis-light curve (*Evans and Parslow*, 1985):

$$f(I) = \frac{\alpha I}{\sqrt{\mu_{max}^2 + \alpha^2 I^2}} \tag{A.5}$$

where α is the initial slope. Nutrient limitations are formulated by Michaelis-Menten functions for nitrate and ammonium (eqs. A.3a- A.3b), and nitrate uptake is taken to be inhibited by the presence of ammonium Parker:1993dr. The parameters k_{NO_3} and k_{NH_4} are half- saturation concentrations for nitrate and ammonium respectively.

The grazing of phytoplankton by zooplankton is given by:

$$g = g_{max} \frac{Phy^2}{k_P + Phy^2} \tag{A.6}$$

where g_{max} is the maximum grazing rate and k_P is the half-saturation of phytoplankton ingestion by zooplankton. Phytoplankton concentration is also lost via mortality defined by the mortality rate m_P, the aggregation of phytoplankton and detritus controlled by parameter τ, and vertical sinking at velocity w_P.

Chlorophyll concentration varies non-linearly with phytoplankton concentration, as pigment concentration per biomass will vary under different light and nutrient conditions in the water column. This non-linearity is introduced through the ratio of achieved photosynthesis ($\mu \cdot Phy$) to the maximum potential photosynthesis ($\alpha \cdot I \cdot Chl$, *Geider et al.*, 1997):

$$\rho_{chl} = \frac{\theta_{max} \mu Phy}{\alpha I Chl} \tag{A.7}$$

The governing equation for the temporal evolution of chlorophyll is derived from that of phytoplankton, multiplied by the ratio of chlorophyll to phytoplankton biomass:

$$\frac{\partial Chl}{\partial t} = \rho_{chl}\mu Chl - gZoo\frac{Chl}{Phy} - m_P Chl - \tau(SDet + Phy)Chl - \frac{\partial}{\partial z}\Big(k_z\frac{\partial Chl}{\partial z}\Big) - w_P Chl \tag{A.8}$$

Zooplankton assimilates ingested phytoplankton with an efficiency β, while the remainder goes to the small detritus pool. Zooplankton loss terms are mortality (at rate m_Z) and excretion. Mortality is proportional to the square of zooplankton biomass. Metabolic and assimilation-dependent excretions are separated in parameters l_M and l_E and both feed into the ammonium pool. The temporal rate of change for zooplankton is given as:

$$\frac{\partial Zoo}{\partial t} = g\beta Zoo - l_M Zoo - l_E\frac{Phy^2}{k_P + Phy^2}\beta Zoo - m_Z Zoo^2 - \frac{\partial}{\partial z}\Big(k_z\frac{\partial Zoo}{\partial z}\Big) \tag{A.9}$$

Small detritus increases in concentration with inefficient zooplankton feeding, and the mortality of zooplankton and phytoplankton. Aggregation of small detritus and phytoplankton feed into the large detritus. Both small and large detritus are remineralized to ammonium at rates r_{SD} and r_{LD} respectively, and both sink at sinking velocities w_S and w_L respectively. The temporal rates of change for small and large detritus are given by:

$$\frac{\partial SDet}{\partial t} = g(1-\beta)Zoo + m_Z Zoo^2 + m_P Phy - \tau(SDet + Phy)SDet - r_{SD}SDet - \frac{\partial}{\partial z}\Big(k_z\frac{\partial SDet}{\partial z}\Big) - w_s\frac{\partial SDet}{\partial z} \tag{A.10}$$

$$\frac{\partial LDet}{\partial t} = \tau(SDet + Phy)^2 - r_{LD}LDet - \frac{\partial}{\partial z}\Big(k_z\frac{\partial LDet}{\partial z}\Big) - w_L\frac{\partial LDet}{\partial z} \tag{A.11}$$

Remineralized detritus go into the ammonium pool, and are then nitrified to feed into the nitrate pool. The nitrification rate n is given by:

$$n = n_{max}\Big(1 - \max\Big[0, \frac{I - I_0}{k_I + I - I_0}\Big]\Big) \tag{A.12}$$

Nitrification is inhibited by light, and so in high intensities drops off to zero per the above equation, where k_I is the half-saturation light level. The time rates of change for model nutrients are given by:

$$\frac{\partial NO_3}{\partial t} = \mu_{max} \cdot f(I) \cdot L_{NO_3} \cdot Phy + nNH_4 - \frac{\partial}{\partial z}\Big(k_z \frac{\partial NO_3}{\partial z}\Big) \tag{A.13}$$

$$\begin{aligned}\frac{\partial NH_4}{\partial t} = &\mu_{max} \cdot f(I) \cdot L_{NH_4} \cdot Phy - nNH_4 + l_M Zoo \\ &+ l_E \frac{Phy^2}{k_P + Phy^2}\beta \cdot Zoo - r_{SD} SDet + r_{LD} LDet - \frac{\partial}{\partial z}\Big(k_z \frac{\partial NH_4}{\partial z}\Big)\end{aligned} \tag{A.14}$$

Finally, oxygen is produced by the growth of phytoplankton, and consumed in the nitrification and remineralization processes, and zooplankton excretion. Air-sea flux is parameterized following *Fennel et al.* (2013a):

$$F_{air-sea} = \frac{vk_{O_2}}{\Delta z}(O_2^{sat} - O_2) \tag{A.15}$$

where O_2^{sat} is the saturation concentration, Δz is the thickness of a model depth layer (0.5 m in this case). The gas exchange coefficient vk_{O_2} (*Wanninkhof*, 1992) is given by:

$$vk_{O_2} = 0.31 u_{10}^2 \sqrt{\frac{660}{Sc_{O_2}}} \tag{A.16}$$

where u_{10} is the wind speed at 10 m above sea level and Sc_{O_2} is the Schmidt number. The temporal evolution of oxygen is governed by the following equation:

$$\begin{aligned}\frac{\partial O_2}{\partial t} = &\mu_{max} \cdot f(I) \cdot (L_{NO_3} R_{O_2:NO_3} + L_{NH_4} R_{O_2:NH_4}) Phy \\ &- 2nNH_4 \\ &- R_{O_2:NH_4}\Big(l_M Zoo + l_E \frac{Phy^2}{k_P + Phy^2}\beta \cdot Zoo + r_{SD} SDet + r_{LD} LDet\Big) \\ &- \frac{\partial}{\partial z}\Big(k_z \frac{\partial O_2}{\partial z}\Big)\end{aligned} \tag{A.17}$$

APPENDIX B

OPTODE FILTER DERIVATION

B.1 Continuous-time DE Solution

Recall filter differential equation:

$$h(t) = f(t) - \tau \frac{\partial h}{\partial t} \tag{B.1}$$

This can be re-written as the following initial value problem, where the initial condition assumes that the initial measurement $y(0)$ is the correct, true value $h(0) = f(0)$:

$$h' + \frac{1}{\tau} h = \frac{1}{\tau} f \qquad h(0) = f(0) \tag{B.2}$$

Taking the LaPlace transform of the above equation, we get:

$$\mathcal{L}\{h' + \frac{1}{\tau} h\} = \mathcal{L}\{\frac{1}{\tau} f\} \tag{B.3}$$

$$sH(s) - h(0) + \frac{1}{\tau} H(s) = \frac{1}{\tau} F(s) \tag{B.4}$$

Re-arranging to solve for $H(s)$ and substituting $h(0) = f(0)$:

$$(s + \frac{1}{\tau})H(s) = f(0) + \frac{1}{\tau}F(s) \tag{B.5}$$

$$H(s) = \Big(\frac{1}{s + \frac{1}{\tau}}\Big)f(0) + \frac{1}{\tau}\Big(\frac{1}{s + \frac{1}{\tau}}\Big)F(s) \tag{B.6}$$

For the first term, we can take the inverse LaPlace transform directly, as we reconize the following form:

$$\mathcal{L}\{\mathrm{e}^{\alpha t}\} = \frac{1}{s - \alpha} \tag{B.7}$$

For the second term, because $x(t)$ is an unknown function, we must write the solution as a convolution. This leaves us with the solution:

$$h(t) = f(0)\mathrm{e}^{-t/\tau} + \frac{1}{\tau}\int_0^t f(t-u)\mathrm{e}^{-u/\tau}du \tag{B.8}$$

B.2 Discretized Filter

Recall filter differential equation:

$$h(t) = f(t) - \tau\frac{\partial h}{\partial t} \tag{B.9}$$

Disretize the differential equation using finite difference:

$$h_n = f_n - \tau\frac{h_n - h_{n-1}}{\Delta t} \tag{B.10}$$

Re-arrange and factor h_n:

$$h_n(1 + \tau\Delta\tau) = f_n + \frac{\tau}{\Delta t}h_{n-1} \tag{B.11}$$

Re-write to solve for h_n:

$$h_n\Big(\frac{\tau+\Delta t}{\Delta t}\Big) = f_n + \frac{\tau}{\Delta t}h_{n-1} \tag{B.12}$$

$$h_n = \Big(\frac{\Delta t}{\tau+\Delta t}\Big)f_n + \Big(\frac{\Delta t}{\tau+\Delta t}\Big)\frac{\tau}{\Delta t}h_{n-1} \tag{B.13}$$

$$h_n = \Big(\frac{\Delta t}{\tau+\Delta t}\Big)f_n + \Big(\frac{\tau}{\tau+\Delta t}\Big)h_{n-1} \tag{B.14}$$

and let $\alpha = \frac{\Delta t}{\tau+\Delta t}$:

$$h_n = \Big(\frac{\Delta t}{\tau+\Delta t}\Big)f_n + \Big(\frac{\tau+\Delta t}{\tau+\Delta t} - \frac{\Delta t}{\tau+\Delta t}\Big)h_{n-1} \tag{B.15}$$

$$h_n = \alpha f_n + (1-\alpha)h_{n-1} \tag{B.16}$$

B.3 Propagation of Error in Deconvolution

Add error into the inverse filtering solution as an addition to the observations h:

$$\frac{f_n + f_{n-1}}{2} = \frac{1}{2b}(h_n - ah_{n-1}) + \frac{1}{2b}(\epsilon_n - a\epsilon_{n-1}) \tag{B.17}$$

where ϵ_n is the error at timestep n. We want to know the coefficient in front of the error term. Assuming that the error ϵ is *i.i.d.*, the variance of this additional term is:

$$\sigma_f^2 = \frac{1+a^2}{4b^2}\sigma_\epsilon^2 \tag{B.18}$$

Replace $a = 1 - 2b$:

$$\frac{1-a^2}{4b^2} = \frac{1+(1-2b^2)^2}{4b^2} \tag{B.19}$$

$$= \frac{1+1-4b+4b^2}{4b^2} \tag{B.20}$$

$$= \frac{2-4b+4b^2}{4b^2} \tag{B.21}$$

$$= \frac{1}{2}b^{-2} - b^{-1} + 1 \tag{B.22}$$

Replace $b^{-1} = 1 + 2\frac{\tau}{\Delta t}$:

$$= \frac{1}{2}\Big(1+2\frac{\tau}{\Delta t}\Big)^2 - \Big(1+2\frac{\tau}{\Delta t}\Big) + 1 \tag{B.23}$$

$$= \frac{1}{2}\Big(1+4\frac{\tau}{\Delta t}+2\frac{\tau^2}{\Delta t^2}\Big) - 1 - 2\frac{\tau}{\Delta t} + 1 \tag{B.24}$$

$$= \frac{1}{2}\Big(1+4\frac{\tau^2}{\Delta t^2}\Big) \tag{B.25}$$

Equation B.25 gives the general result, and the variance of the error will by multiplied by that factor. The standard deviation therefore is amplified by the following factor:

$$\frac{\sigma_f}{\sigma_\epsilon} = \sqrt{\frac{1}{2}\Big(1+4\frac{\tau^2}{\Delta t^2}\Big)} \tag{B.26}$$

For our model experiment, $\tau = 75\,\mathrm{s}$ and $\Delta t = 33\,\mathrm{s}$. The amplification of the standard deviation will be the square root of the above which shows the amplification of the variance:

$$\sqrt{\frac{1}{2}\Big(1+4\frac{\tau^2}{\Delta t^2}\Big)} = \sqrt{\frac{1}{2}\Big(1+4\frac{(75\,\mathrm{s})^2}{(33\,\mathrm{s})^2}\Big)} \tag{B.27}$$

$$\approx 3.3 \tag{B.28}$$

The above does not account for any smoothing.

BIBLIOGRAPHY

Alford, M. H., J. A. MacKinnon, H. L. Simmons, and J. D. Nash, Near-Inertial Internal Gravity Waves in the Ocean, *Annual Review of Marine Science*, *8*, 95–123, 2016. 49, 50, 59

Antoniou, A., *Digital filters: analysis, design, and signal processing applications*, 2 ed., 2018. 26

Bagniewski, W., K. Fennel, M. J. Perry, and E. A. D'Asaro, Optimizing models of the North Atlantic spring bloom using physical, chemical and bio-optical observations from a Lagrangian float, *Biogeosciences*, *8*, 1291–1307, 2011. 19

Behrenfeld, M. J., and P. G. Falkowski, Photosynthetic rates derived from satellite-based chlorophyll concentration, *Limnol. Oceanogr.*, *42*, 1997. 2, 5, 41, 42

Bennett, A. S., and T. Huaide, CTD time-constant correction, *Deep Sea Research Part A. Oceanographic Research Papers*, *33*, 1425–1438, 1986. 17

Bianchi, T. S., S. F. DiMarco, J. H. Cowan, R. D. Hetland, P. Chapman, J. W. Day, and M. A. Allison, The science of hypoxia in the Northern Gulf of Mexico: a review., *Science of The Total Environment*, *408*, 1471–1484, 2010. 7

Bittig, H. C., and A. Körtzinger, Technical Note: Oxygen Optodes on Profiling Platforms: Update on Response Times, In-Air Measurements, and In-Situ Drift, *Ocean Science Discussions*, 2016. 4, 16, 17, 27, 29, 37

Bittig, H. C., B. Fiedler, R. Scholz, G. Krahmann, and A. Körtzinger, Time response of oxygen optodes on profiling platforms and its dependence on flow speed and temperature, *Limnol. Oceanogr.*, *12*, 617–636, 2014. 4, 17, 36, 37

Bittig, H. C., B. Fiedler, P. Fietzek, and A. Körtzinger, Pressure Response of Aanderaa and Sea-Bird Oxygen Optodes, *Journal of Atmospheric and Oceanic Technology*, *32*, 2305–2317, 2015. 4, 15

Bittig, H. C., A. Körtzinger, C. Neill, E. van Ooijen, J. N. Plant, J. Hahn, K. S. Johnson, B. Yang, and S. R. Emerson, Oxygen Optode Sensors: Principle, Characterization, Calibration, and Application in the Ocean, *Frontiers in Marine Science*, *4*, 1–25, 2018. 4, 17, 37

Boas, M. L., *Mathematical Methods in the Physical Sciences*, 3 ed., Wiley, 2006. 25

Bopp, L., L. Resplandy, J. C. Orr, S. C. Doney, J. P. Dunne, M. Gehlen, P. Halloran, C. Heinze, T. Ilyina, R. Séférian, J. Tjiputra, and M. Vichi, Multiple stressors of ocean ecosystems in the 21st century: Projections with CMIP5 models, *Biogeosciences*, *10*, 6225–6245, 2013. 7

Boyd, P. W., S. T. Lennartz, D. M. Glover, and S. C. Doney, Biological ramifications of climate-change-mediated oceanic multi-stressors, *Nature Climate Change*, *5*, 71–79, 2015. 7

Briggs, N., M. J. Perry, I. Cetinić, C. Lee, E. D'Asaro, A. M. Gray, and E. Rehm, High-resolution observations of aggregate flux during a sub-polar North Atlantic spring bloom, *Deep-Sea Research Part I*, *58*, 1031–1039, 2011. v, 14, 15

Briggs, N., K. Guðmundsson, I. Cetinić, E. D'Asaro, E. Rehm, C. Lee, and M. J. Perry, A multi-method autonomous assessment of primary productivity and export efficiency in the springtime North Atlantic, *Biogeosciences*, *15*, 4515–4532, 2018. 3, 4, 5, 41, 44, 48

Bushinsky, S. M., S. R. Emerson, S. C. Riser, and D. D. Swift, Accurate oxygen measurements on modified Argo floats using in situ air calibrations, *Limnology and Oceanography: Methods*, *14*, 491–505, 2016. 4

Caffrey, J. M., Production, respiration and net ecosystem metabolism in U.S. estuaries., *Environmental Monitoring and Assessment*, *81*, 207–219, 2003. 3

Carpenter, J. H., The Chesapeake Bay Institute Technique for the Winkler Dissolved Oxygen Method, *Limnology and Oceanography*, *10*, 141–143, 1965. 36

Cassar, N., B. A. Barnett, M. L. Bender, J. Kaiser, R. C. Hamme, and B. Tilbrook, Continuous High-Frequency Dissolved O_2/Ar Measurements by Equilibrator Inlet Mass Spectrometry, *Analytical Chemistry*, *81*, 1855–1864, 2009. 2

Claustre, H., A. Morel, M. Babin, C. Cailliau, D. Marie, J.-C. Marty, D. Tailliez, and D. Vaulot, Variability in particle attenuation and chlorophyll fluorescence in the tropical Pacific: Scales, patterns, and biogeochemical implications, *Journal of Geophysical Research: Oceans*, 1999. 3

Cullen, J. J., Subsurface Chlorophyll Maximum Layers: Enduring Enigma or Mystery Solved?, *Annual Review of Marine Science*, *7*, 207–239, 2015. 57

Cullen, J. J., P. J. Neale, and M. P. Lesser, Biological weighting function for the inhibition of phytoplankton photosynthesis by ultraviolet radiation, *Science*, *258*, 646–650, 1992. 3

Dall'Olmo, G., E. Boss, M. J. Behrenfeld, and 2011, Inferring phytoplankton carbon and eco-physiological rates from diel cycles of spectral particulate beam-attenuation coefficient, *Biogeosciences*, 2011. 3

Ducklow, H. W., and S. C. Doney, What Is the Metabolic State of the Oligotrophic Ocean? A Debate, *Annual Review of Marine Science*, *5*, 525–533, 2013. 41

Eppley, R. W., Temperature and phytoplankton growth in the sea, *Fishery Bulletin*, *70*, 1063–1085, 1972. 64

Evans, G. T., and J. S. Parslow, A model of annual plankton cycles, *Biological Oceanography*, *3*, 327–347, 1985. 65

Fennel, K., J. Wilkin, J. Levin, J. Moisan, J. O'Reilly, and D. Haidvogel, Nitrogen cycling in the Middle Atlantic Bight: Results from a three-dimensional model and implications for the North Atlantic nitrogen budget, *Global Biogeochemical Cycles*, *20*, 2006. 18

Fennel, K., J. Hu, A. Laurent, M. M. Almeida, and R. Hetland, Sensitivity of hypoxia predictions for the northern Gulf of Mexico to sediment oxygen consumption and model nesting, *Journal of Geophysical Research: Oceans*, *118*, 990–1002, 2013a. 67

Fennel, K., J. Hu, A. Laurent, M. Marta-Almeida, and R. Hetland, Sensitivity of hypoxia predictions for the northern Gulf of Mexico to sediment oxygen consumption and model nesting, *Journal of Geophysical Research: Oceans*, *118*, 990–1002, 2013b. 7

Geider, R. J., H. L. MacIntyre, and T. M. Kana, Dynamic model of phytoplankton growth and acclimation: responses of the balanced growth rate and the chlorophyll a:carbon ratio to light, nutrient-limitation and temperature, *Marine Ecology Progress Series*, *148*, 187–200, 1997. 65

Gernez, P., D. Antoine, and Y. Huot, Diel cycles of the particulate beam attenuation coefficient under varying trophic conditions in the northwestern Mediterranean Sea: Observations and modeling, *Limnol. Oceanogr.*, *56*, 17–36, 2010. 3

Gruber, N., S. C. Doney, S. R. Emerson, D. Gilbert, T. Kobayashi, and A. Körtzinger, Adding Oxygen to Argo: Developing a Global In Situ Observatory for Ocean Deoxygenation and Biogeochemistry., *Proceedings of OceanObs Sustained Ocean Observations and Information for Society*, 2010. 4

Hamme, R. C., N. Cassar, V. P. Lance, R. D. Vaillancourt, M. L. Bender, P. G. Strutton, T. S. Moore, M. D. DeGrandpre, C. L. Sabine, D. T. Ho, and B. R. Hargreaves, Dissolved O_2/Ar and other methods reveal rapid changes in productivity during a Lagrangian experiment in the Southern Ocean, *Journal of Geophysical Research: Oceans*, *117*, 2012. 2

Johnson, K. S., J. N. Plant, S. C. Riser, and D. Gilbert, Air Oxygen Calibration of Oxygen Optodes on a Profiling Float Array, *Journal of Atmospheric and Oceanic Technology*, *32*, 2160–2172, 2015. 4, 15

Johnson, K. S., J. N. Plant, L. J. Coletti, H. W. Jannasch, C. M. Sakamoto, S. C. Riser, D. D. Swift, N. L. Williams, E. Boss, N. Haëntjens, L. D. Talley, and J. L. Sarmiento, Biogeochemical sensor performance in the SOCCOM profiling float array, *Journal of Geophysical Research: Oceans*, *122*, 6416–6436, 2017. 16, 35, 36

Kaiser, J., M. K. Reuer, B. Barnett, and M. L. Bender, Marine productivity estimates from continuous O2/Ar ratio measurements by membrane inlet mass spectrometry, *Geophysical Research Letters*, *32*, 2005. 2

Kautsky, H., Quenching of luminescence by oxygen, *Transactions of the Faraday Society*, *35*, 216–219, 1939. 14

Kinkade, C. S., J. Marra, T. D. Dickey, C. Langdon, D. E. Sigurdson, and R. Weller, Diel bio-optical variability observed from moored sensors in the Arabian Sea, *Deep Sea Research Part II Topical Studies in Oceanography*, 1999. 3

Kuhn, A. M., K. Fennel, and J. P. Mattern, Model investigations of the North Atlantic spring bloom initiation, *Progress in Oceanography*, *138*, 176–193, 2015. 19

Lagman, K. B., K. Fennel, K. R. Thompson, and L. Bianucci, Assessing the utility of frequency dependent nudging for reducing biases in biogeochemical models, *Ocean Modelling*, *81*, 25–35, 2014. 18

Muller-Karger, F. E., J. P. Smith, S. Werner, R. Chen, M. Roffer, Y. Liu, B. Muhling, D. Lindo-Atichati, J. Lamkin, S. Cerdeira-Estrada, and D. B. Enfield, Natural variability of surface oceanographic conditions in the offshore Gulf of Mexico, *Progress in Oceanography*, *134*, 54–76, 2015. 8

Nicholson, D. P., and M. L. Feen, Air calibration of an oxygen optode on an underwater glider, *Limnology and Oceanography: Methods*, *15*, 495–502, 2017. 4

Nicholson, D. P., S. T. Wilson, S. C. Doney, and D. M. Karl, Quantifying subtropical North Pacific gyre mixed layer primary productivity from Seaglider observations of diel oxygen cycles, *Geophysical Research Letters*, pp. 4032–4039, 2015. 3, 5, 41, 48, 49, 59

Omand, M. M., I. Cetinić, and A. J. Lucas, Using bio-optics to reveal phytoplankton physiology from a Wirewalker autonomous platform, *Oceanography*, 2017. 3

Plant, J. N., K. S. Johnson, C. M. Sakamoto, H. W. Jannasch, L. J. Coletti, S. C. Riser, and D. D. Swift, Net community production at Ocean Station Papa observed with nitrate and oxygen sensors on profiling floats, *Global Biogeochemical Cycles*, *30*, 859–879, 2016. 35, 36, 49, 59

Proakis, J. G., and D. G. Monolakis, *Digital Signal Processing: Principles, Algorithms, and Applications*, 3 ed., Prentice-Hall International, 1996. 26

Riser, S. C., and K. S. Johnson, Net production of oxygen in the subtropical ocean., *Nature*, *451*, 323–325, 2008. 3, 49

Roesler, C., J. Uitz, H. Claustre, E. Boss, X. Xing, E. Organelli, N. Briggs, A. Bricaud, C. Schmechtig, A. Poteau, F. D'Ortenzio, J. Ras, S. Drapeau, N. Haëntjens, and M. Barbieux, Recommendations for obtaining unbiased chlorophyll estimates from in situ chlorophyll fluorometers: A global analysis of WET Labs ECO sensors, *Limnology and Oceanography: Methods*, *15*, 572–585, 2017. 12

Roesler, C. S., and A. H. Barnard, Optical proxy for phytoplankton biomass in the absence of photophysiology: Rethinking the absorption line height, *Methods in Oceanography*, *7*, 79–94, 2013. 12

Schmechtig, C., A. Poteau, H. Claustre, F. D'Ortenzio, and E. Boss, Processing Bio-Argo chlorophyll-a concentration at the DAC level, 2015. 12

Schmechtig, C., A. Poteau, H. Claustre, F. D'Ortenzio, G. Dall'Olmo, and E. Boss, Processing BGC-Argo particle backscattering at the DAC level, 2018. 14

Steeman-Nielsen, E., The use of radio-active carbon (C^{14}) for measuring organic production in the sea, *ICES Journal of Marine Science*, *18*, 117–140, 1952. 1

Tengberg, A., J. Hovdenes, H. J. Andersson, O. Brocandel, R. Diaz, D. Hebert, T. Arnerich, C. Huber, A. Körtzinger, A. Khripounoff, F. Rey, C. Rönning, J. Schimanski, S. Sommer, and A. Stangelmayer, Evaluation of a lifetime-based optode to measure oxygen in aquatic systems, *Limnology and Oceanography: Methods*, *4*, 7–17, 2006. v, 4, 16

Thierry, V., H. Bittig, D. Gilbert, T. Kobayashi, K. Sato, and C. Schmid, Processing Argo OXYGEN data at the DAC level, pp. 1–134, 2016. 15

Tortell, P. D., E. C. Asher, H. W. Ducklow, J. A. L. Goldman, J. W. H. Dacey, J. J. Grzymski, J. N. Young, S. A. Kranz, K. S. Bernard, and F. M. M. Morel, Metabolic balance of coastal Antarctic waters revealed by autonomous pCO2 and ΔO2/Ar measurements, *Geophysical Research Letters*, *41*, 6803–6810, 2014. 2

Wanninkhof, R., Relationship between wind speed and gas exchange over the ocean, *Journal of Geophysical Research*, *97*, 7373–7382, 1992. 58, 67

Westberry, T., M. J. Behrenfeld, D. A. Siegel, and E. Boss, Carbon-based primary productivity modeling with vertically resolved photoacclimation, *Global Biogeochemical Cycles*, *22*, 2008. 2

Westberry, T. K., P. J. le B Williams, and M. J. Behrenfeld, Global net community production and the putative net heterotrophy of the oligotrophic oceans, *Global Biogeochemical Cycles*, *26*, n/a–n/a, 2012. 41

White, A. E., B. Barone, R. M. Letelier, and D. M. Karl, Productivity diagnosed from the diel cycle of particulate carbon in the North Pacific Subtropical Gyre, *Geophysical Research Letters*, *44*, 3752–3760, 2017. 3

Wiener, N., *Extrapolation, Interpolation, and Smoothing of Stationary Time Series*, The MIT Press, 1964. 27

Winkler, L., The determination of dissolved oxygen in water, *Ber. Deutsch Chem. Gos.*, *21*, 2843–2855, 1888. 36

Xing, X., H. Claustre, S. Blain, F. D'Ortenzio, D. Antoine, J. Ras, and C. Guinet, Quenching correction for in vivo chlorophyll fluorescence acquired by autonomous platforms: A case study with instrumented elephant seals in the Kerguelen region (Southern Ocean), *Limnology and Oceanography: Methods*, *10*, 483–495, 2012. 12, 13

Yu, L., K. Fennel, and A. Laurent, A modeling study of physical controls on hypoxia generation in the northern Gulf of Mexico, *Journal of Geophysical Research: Oceans*, *120*, 5019–5039, 2015. 7

Zhang, X., L. Hu, and M.-X. He, Scattering by pure seawater: Effect of salinity, *Optics Express*, *17*, 5698, 2009. 14